Arab American University-Jenin

Faculty of Graduate Studies

Post annealing effects and in situ monitoring of the phase transitions in $CdBr_2$ powders.

By

Amaal Moustafa Najah Weshahe

Supervisor

Prof. Dr. Atef Qasrawi

This thesis was submitted in partial fulfillment of the requirement for the Master's degree in

Physics

October/2020.

Post annealing effects and in situ monitoring of the phase transitions in $CdBr_2$ powders

By

Amaal Moustafa Najah Weshahe

This thesis was defended successfully on October 2020 and approved by:

Committee members	Signature
1. Prof. Dr. Atef Fayez Qasrawi (Supervisor)	……..
2. Prof. Dr. Hazem Khanfar	……..
3. Dr. Iyad Saadeddin	……..

Declaration

The work in this thesis, unless otherwise referenced, is the researcher's own work and has not been submitted elsewhere for any other degree or qualification.

العمل في هذه الرسالة، ما لم تتم الاشارة الى خلاف ذلك، هو عمل الباحث الخاص ولم يتم تقديمه في أي مكان آخر للحصول على درجة أو مؤهل آخر.

Student's Name: **Amaal Moustafa Najah Weshahe.**

Signature:

Date:

To

my

parents

Acknowledgments

The first and final thanks to Almighty Allah after that, I would like to express my deepest gratitude to my family and my fiancé who stand behind me and supported me every time to pass this degree. I am grateful for who helped me through my life. To whom taught me, everyone who encouraged me to be strong in my education and complete my educational career.

Thanks to all teaching members along my life until today, from schools to Arab American University, especially thanks to my supervisor Prof. Dr. Atef Qasrawi, the science and research lab assistant Olfat Omaryeh and Rana Daraghmeh.

Abstract

Post annealing effects and in situ monitoring of the phase transitions in $CdBr_2$ powders

By

Amaal Moustafa Najah Weshahe

Supervisor

Prof. Dr. Atef Qasrawi

In this thesis, we focused on studying the in situ heating and post annealing effects, on the structural, optical and electrical properties of $CdBr_2$ powders. The powders were subjected to an in situ heating processes in the temperature range of 20-200 °C. For these samples, before heating, multistructural phases existed. The most dominant structural phase was the triclinic. The heating cycle resulted in a relaxation of the crystal structural parameters and changed the dominant phase from triclinic to hexagonal. The structure transfer is accompanied with changes in crystallite size, strain, defect density and increased the stacking faults percentage.

On the other hand, when $CdBr_2$ powders were heat treated at elevate temperatures of 200 °C, 300 °C and 400 °C for one hour in rough vacuum media. The structural properties were different. Namely, the phase weight of the triclinic structure decreased from 68.3% to 53.9%, 46.0% and reached 13.7% as the annealing temperature increased from 25 °C, to 200 °C, 300 °C and reaches 400 °C, respectively. The most dominant structural phase for the samples annealed at 400 °C was monoclinic.

The annealing cycle altered the lattice parameters, slightly enhanced the crystallite size and the microstrain. It is also decreased the defect density without altering the stacking fault percentages.

The optical investigations on the as grown and heat treated samples have shown that the transparency of the powders in the ultraviolet range increases with increasing molar concentration and increasing

annealing temperature. The energy band gap decreased from 5.11 eV to 5.10 eV as the annealing temperature increased from 25 °C to 400 °C.

The electrical measurements have shown that the annealing process increases the electrical resistance of the identical samples. While the as grown samples displayed two resonance- antiresonance peaks in the radio and microwave ranges of spectrum, the samples annealed at 200 °C and 400 °C displayed one peak in the microwave range. The higher the annealing temperature, the larger the resonance frequency. The capacitance spectra display negative values near the resonance peaks. Consistently, the conductance spectra show negative conductance effect indicating the dominant of the tunneling process in the annealed samples. Measurements of the reflection coefficient magnitude for as grown and annealed powders in the microwave range have shown the applicability of the samples as band pass filters operating above 1.5 GHz.

List of contents

List of tables

List of figures

Chapter One

Introduction

Cadmium bromide ($CdBr_2$) has newly attracted the attention of researchers and electronic device designers. Recent reports indicate the possibility of using this material to investigate the effect of the position of the Fluoride atom in the aniline ring. The position of the atom affects the crystal structure and interrupt its thermal stability. [1]. In addition, studies on Mn-doped CdS/$CdBr_2$ hetero-nanostructures provided promising templates for constructing high-performance optoelectronic devices. This device has a hexagonal plate on top of a nanowire, and prepared by a simple one-step thermal evaporation process [2]. In addition, $CdBr_2$ was crystallized with 4-hydroxy-L-proline in a non-Centro symmetric space group *via* a slow evaporation solution method. The metal-organic compound is used in non-linear optical (NLO) applications [3]. $CdBr_2$ have antibacterial applications [4]. $CdBr_2$ powders also find applications as infrared detectors and emitters, thermoelectric materials, technical field infrared laser and the like [5]. On the other hand, $CdBr_2$ has been synthesized as mechanical energy harvesting devices. These devices made up of organic-nonorganic hybrid materials embedded in poly- dimethylsiloxane (PDMS). The energy harvested from these devices was used to charge a capacitor through a full-bridge rectifier [6]. CdTe which was treated with a $CdBr_2$ show reduction in defect densities [7].

$CdBr_2$ powders have been prepared by various techniques including vapor-phase reactions, liquid solutions, and solid state reaction techniques (SSR). This technique has an advantage that structural elements can be maintained in the transformation from reactant to product. In addition, the solid reactants react chemically without a presence of any solvent at high temperatures, giving a stable and pure structured material.

$CdBr_2$ it is a white to yellowish crystalline powders. It has property that distinguishes it from others such as it is melting temperature is 568° C, boiling temperature is 863° C, and density is 5.19 g/cm^3 [8]. These properties make it freely soluble in water and alcohol; moderately soluble in acetone, slightly soluble in ether. However, the structural reports indicated the possible existence of more than one structural phase at a time in these powders.

Cadmium bromide crystallized in an ionic layer type structure, namely, the rhombohedral structure, in which each cadmium ion layer is sandwiched by two bromine ions layers. A cadmium ion is located at the center of an octahedron composed of six nearest neighbor bromide ions. The binding within the layer is strong with a high ionic interaction, while binding between the sheets is weak. The top of the valence band composed of bromine p orbits while the bottom of the conduction band basically of cadmium 5s orbits. The lowest optical excitation absorption band is located at 4.96 eV. Optical excitation in the fundamental absorption region produces two emission bands in near Ultraviolet (UV:3.30 eV) and yellow (Y:2.20 eV) regions [9]. They are attributed to the self-trapped excitation luminescence.

$CdBr_2$ compound is known for its potential application as media suitable for lasing and quantum dot light emitting diode fabrication. For these important sectors of applications, optimizing stable structure is very necessary for long life working machines. It is observed that studies on the phase transitions and structural stability in these powders are very rare in literature. For this reason, here in this work we target monitoring the structural transitions and stability in the powders to state the optimum structure and optimum structural parameters. Particularly, we target monitoring the temperature and annealing effects on the grain size, macrostrain and stress, defect density and stacking faults in the powders. In addition, computer simulations with the help of "TREOR 92" software packages will be carried out to determine the effect temperature and annealing on the

plane orientations and lattice parameters of the crystalline powders. The Schematics of the crystal phases before and after heating will be constructed. Moreover, the optical properties for the $CdBr_2$ powders and annealed powders will be studied at different molar concentrations 0.1 M, 0.2 M and 0.3 M. In addition, the impedance and Current-voltage characteristics will be seen for as grown and annealed $CdBr_2$ powders at 200 °C, 300 °C and 400 °C.

In this thesis, the theoretical background will be discussed in the second chapter. The experimental details and procedures in the third chapter. In the fourth chapter, the results will be seen from the x-ray diffraction, optical spectroscopy, the impedance spectroscopy in the microwave range and Current-voltage characteristics for the as grown and annealed $CdBr_2$ powders. Finally, concluding remarks will be considered in the fifth chapter.

Chapter Two

Theoretical Background

2.1 X-rays diffraction (XRD) analysis:

X-rays diffraction (XRD) is a nondestructive technique to identify crystalline phases and orientation. In 1912, X-ray diffraction was discovered by Laue and his co-workers, it is an experimental evidence for the periodicity of the structure, that the index numbers that define the orientations of the faces of a crystal are exact integers [10].

2.1.1: Lattice Crystal structures

A crystal is constructed by the infinite repetition of identical groups of atoms. A group is called a basis. The set of mathematical points which attached to a basis are called the lattice. The lattice in 3-dimensions can be defined by three translational vectors $\boldsymbol{a_1}, \boldsymbol{a_2}$ *and* $\boldsymbol{a_3}$. The set of points $\mathbf{r}$ defined by

$$\boldsymbol{r} = \mathrm{u}_1\mathbf{a_1} + \mathrm{u}_2\boldsymbol{a_2} + u_3\boldsymbol{a_3} \qquad (2.1)$$

Where u_1, u_2 and u_3 are arbitrary integers.

The crystal structures were divided into seven groups of cells according to their point groups and their Braves lattices, which are cubic, hexagonal, trigonal, tetragonal, orthorhombic, monoclinic and triclinic. The division of structures are shown in table (2.1) in terms of the axial relations that describe the cells [10].

The orientation of the crystal plane is determined by three points in the plane. If each point lay on a different crystal axis, the plane could be specified by giving the coordinates of the points in terms of the lattice constants a_1, a_2 *and* a_3. The orientation of a plane is specified by the miller indices (h, k, l) that determined by finding the intercepts on the axes $\boldsymbol{a_1}, \boldsymbol{a_2}$ *and* $\boldsymbol{a_3}$, then taking the

reciprocals of these intercepts and reducing them to three integers having the same ratio. The result is called the index of the plane ($h\ k\ l$) [10].

Table 2.1: The seven lattice groups in three dimensions

System	Number of lattices	Axial distances and angles
Cubic	3	$a = b = c$ $\alpha = \beta = \gamma = 90^{\circ}$
Hexagonal	1	$a = b \neq c$ $\alpha = \beta = 90^{\circ}, \gamma = 120^{\circ}$
Trigonal	1	$a = b = c$ $\alpha = \beta = \gamma < 120^{\circ}, \neq 90^{\circ}$
Tetragonal	2	$a = b \neq c$ $\alpha = \beta = \gamma = 90^{\circ}$
Orthorhombic	4	$a \neq b \neq c$ $\alpha = \beta = \gamma = 90^{\circ}$
Monoclinic	2	$a \neq b \neq c$ $\alpha = \gamma = 90^{\circ} \neq \beta$
Triclinic	1	$a \neq b \neq c$ $\alpha \neq \beta \neq \gamma$

Each system has an interplanar spacing d which is related to the unit cell dimensions and Miller indices. This amount is the spacing between two adjacent parallel planes.

The reciprocal lattice vectors define a vector space which enables many useful geometric calculations in crystallography, such as finding the relations for the interplanar angles, spacing and cell volume for the non-cubic systems. The crystal lattice constructed with a unit vectors which is associated with some periodic structure are called the reciprocal lattice. Note that the reciprocal vectors have dimensions of inverse length.

Points in the reciprocal lattice are mapped by the set of vectors

$$d^*_{hkl} = ha^* + kb^* + lc^* \qquad (2.2)$$

Where h, k, l are integers. A vector d^*_{hkl} is a reciprocal lattice vector.

And also,

$$a^* = \frac{b \times c}{a.\, b \times c} \quad , \quad b^* = \frac{c \times a}{a.\, b \times c} \quad , \quad c^* = \frac{a \times c}{a.\, b \times c} \qquad (2.3)$$

Where a, b, c are the primitive vectors of the crystal lattice.

Now, we will start to derive the spacing interplanar for the triclinic structure. Which there is no relationships between the lattice parameters $(a \neq b \neq c)$ and lattice angles$(\alpha \neq \beta \neq \gamma)$, in order to reach the formula for the other structures.

$$\begin{aligned} d^*_{hkl}.\, d^*_{hkl} &= (ha^* + kb^* + lc^*).\,(ha^* + kb^* + lc^*) \\ &= h^2a^{*2} + k^2b^{*2} + l^2c^{*2} + 2hka^*b^*cos\gamma^* + 2klb^*c^*cos\alpha^* \\ &\quad + 2hlc^*a^*cos\beta \end{aligned} \qquad (2.4)$$

Then the spacing interplanar can be written as

$$\frac{1}{d_{hkl}^2} = h^2b^2c^2\left(\frac{\sin^2\alpha}{V^2}\right) + k^2a^2c^2\left(\frac{\sin^2\beta}{V^2}\right) + l^2b^2a^2\left(\frac{\sin^2\gamma}{V^2}\right)$$
$$+ \ 2hkabc^2\left(\frac{cos\alpha\ cos\beta - cos\gamma}{V^2}\right) + 2klbca^2\left(\frac{cos\gamma\ cos\beta - cos\alpha}{V^2}\right)$$
$$+ 2hlacb^2\left(\frac{cos\gamma\ cos\beta - cos\alpha}{V^2}\right)$$

Substitute the value of V in the previous equation, where V is the volume of the lattice $= a.b \times c$.

Finally, one can get the spacing interplanar for the triclinic lattice as

$$\frac{1}{d_{hkl}^2} = \frac{\begin{bmatrix} h^2b^2c^2\sin^2\alpha + k^2a^2c^2\sin^2\beta + l^2b^2a^2\sin^2\gamma \\ +\ 2hkabc^2(cos\alpha\ cos\beta - cos\gamma) + 2klbca^2(cos\gamma\ cos\beta - cos\alpha) \\ +2hlacb^2(\ cos\gamma\ cos\beta - cos\alpha) \end{bmatrix}}{1 - \cos^2\alpha - \cos^2\beta - \cos^2\gamma + 2cos\alpha\ cos\beta\ cos\gamma} \qquad (2.5)$$

By using the equation (2.5) and table (2.1), one can derive all other interplanar spacing. The interplanar spacing relations are summarized in table 2.2.

Table 2.2: The interplanar spacing formula for the other six structures than triclinic

crystal System	Spacing Interplanar
Cubic	$\frac{1}{d^2} = \frac{(h^2+k^2+l^2)}{a^2}$
Hexagonal	$\frac{1}{d^2} = \frac{4}{3a^2}(h^2+hk+k^2) + \frac{l^2}{c^2}$
Trigonal	$\frac{1}{d^2} = \frac{4}{3a^2}(h^2+hk+k^2) + \frac{l^2}{c^2}$
Tetragonal	$\frac{1}{d^2} = \frac{1}{a^2}(h^2+k^2) + \frac{l^2}{c^2}$
Orthorhombic	$\frac{1}{d^2} = \frac{h^2}{a^2} + \frac{k^2}{b^2} + \frac{l^2}{c^2}$
Monoclinic	$\frac{1}{d^2} = \frac{h^2}{a^2\sin^2\beta} + \frac{k^2}{b^2} + \frac{l^2}{c^2\sin^2\beta} - \frac{2hlcos\beta}{ac\sin^2\beta}$

2.1.2: Bragg's law

The structure of crystal is studied by the diffraction of photons and electrons. The diffraction depends on the structure of the crystal and on the wavelength. Lawrence Bragg presented a simple explanation of the diffracted beams from a crystal. For a crystalline solid, the waves are scattered from lattice planes separated by the lattice planes spaced d. When the constructive interference occurred, the waves remain in phase since the differences in the travel path must be equal to multiple integers of the wavelength. The path difference between two adjacent planes is 2d sin θ (Fig. 2.1). So that

$$2d\ sin\theta = n\lambda \qquad (2.6)$$

Where d is the spacing between the crystal planes of a given specimen, θ is the glancing angle, n is the order of diffraction, and λ is the wavelength of x-rays in our work λ = 1.5405 A°. By measuring the angles (θ), under which the constructively interfering x-rays leave the crystal, the interplanar crystal spacing (d) of every single crystallographic phase can be determined.

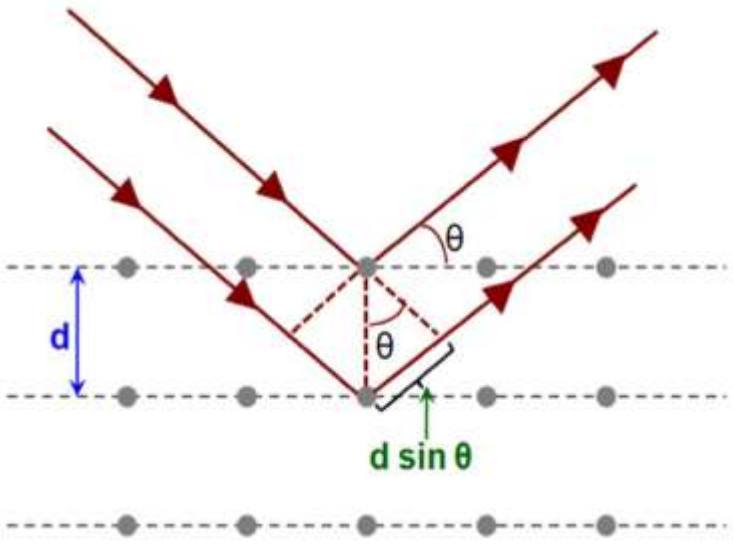

Figure 2.1: Condition for diffraction and derivation of Bragg's law.

2.1.3: Structural Parameters

XRD gives information about the structural parameters, like as crystalline size (D), lattice strain (ε), dislocation density (δ), and stacking faults (SF %) [11]. Broadening of x-rays diffracted peaks enables the calculation of the crystalline size and lattice strains. Crystalline size (D) is calculated using the Scherrer formula

$$D = \frac{K\lambda}{\beta cos\theta} \qquad (2.7)$$

Where D is the measure of the dimension of the particle, K is a constant taken as 0.94, (most popular), λ is the wavelength of the x-ray, and θ is the Bragg's angle.β is the full width at half maximum (FWHM) measured in radians, it can be calculated as can be seen from Fig.2.1:

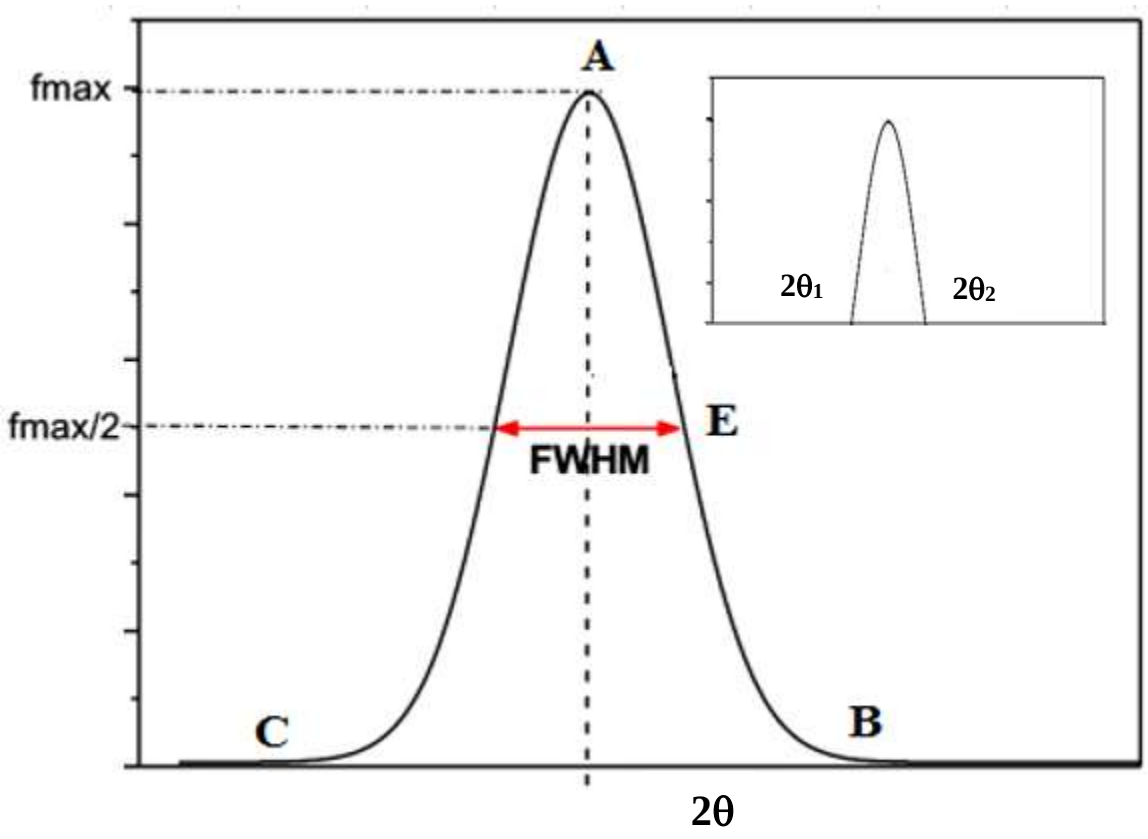

Figure 2.2: Full width of high maxima.

$$D = \frac{B + C}{2} \qquad (2.8)$$

$$E = \frac{A - D}{2} \qquad (2.9)$$

Position of full width high maxima (FWHM) $= E + D$

Then we can get b from following equation:

$$\beta = (|2\theta_2 - 2\theta_1|) \times \left(\frac{3.14}{180}\right) \qquad (2.10)$$

Lattice strain is the ratio of contraction or expansion in bonds lengths to the original bonds lengths, it is measured by the following equation:

$$\varepsilon = \frac{\beta}{4tan\theta} \qquad (2.11)$$

The dislocation density is defined as the length of the dislocation lines per unit area of the crystal, and could be calculated by the following equation:

$$\delta = \frac{15\varepsilon}{aD} lines/cm^2 \qquad (2.12)$$

Where ε is the strain, a is the lattice constant and D is the crystallite size.

The stacking faults represents error in the regular sequence of layers of crystallographic planes.

$$SF\% = \frac{2\pi^2\beta}{45\sqrt{3tan\theta}} \times 100\% \qquad (2.13)$$

2.1.4: Deformation in materials

The free energy of a crystalline materials is increased during deformation due to the presence of dislocation and interfaces. A material which contains these defects is thermodynamically unstable. If the material is heated to high temperatures (annealed), the microstructures and the properties of the material are altered. The most clearly change in this case is that the grains shape will change, which lead to an increase in the area of the total grain boundary. So, more strain and dislocations

are present in the material, and so the stored energy will increase. In addition, when crystal is deformed the internal structure of the grains may appear due to the accumulation of dislocations because of the interstitials or vacancies in the material [12].

2.2: Optical properties

Optical properties of materials are very important in the development of technology. These properties depend on how the electromagnetic radiation interacts with material. This interaction is due to the wavelength and frequency of the radiation beam and also the property of the material like refractive index, dielectric constant, band gap values, etc. These optical properties affected by the macroscopic and microscopic properties of the material, like the nature of its surface and its electronic structure. There are many optical properties, the most important: reflection, refraction, transmission and absorption.

2.2.1 Band to band or fundamental absorption:

Band to band or fundamental absorption of radiation returns to the photoexcitation of an electron from the valence band (VB) to the conduction band (CB). There are two types of band to band absorption, which are direct and indirect transitions.

2.2.1.1 Direct transition:

A direct transition is a photoexcitation process in which no phonons are involved. The photon momentum very little compared with the electron momentum, so when the photon of energy (hv) is absorbed, electron excited from VB to CB, the electron's k vector does not change [13]. A direct

transition on $E - k$ diagram is a vertical transition from an initial energy E and wave vector k in the VB to a final energy E' and a wave vector k'in the CB where $k' = k$, as shown in Fig. 2.3.

$$E' - E_C = \frac{P^2}{2m_e^*} = \frac{(\hbar k)^2}{2m_e^*} \qquad (2.14)$$

$$E_v - E = \frac{(\hbar k)^2}{2m_h^*} \qquad (2.15)$$

The ratio of the kinetic energies of the photo generated electron and hole depends inversely on the ratio of their effective masses.

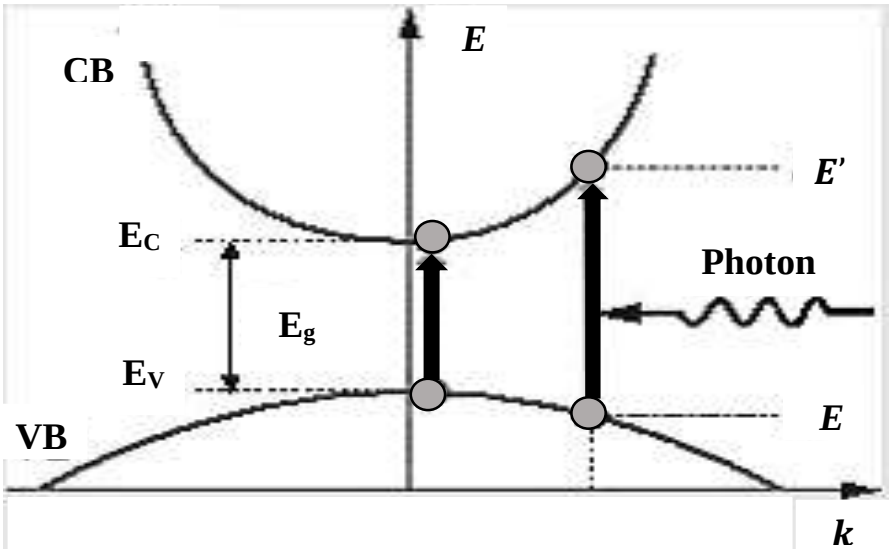

Figure 2.3: A direct transition from VB to CB through the absorption of a photon.

The absorption coefficient α is derived from the quantum mechanical probability of transition from E to E', the occupied density of states at E in the VB from which electrons are excited, and the unoccupied density of states in the CB at $E + h\nu$. Near the band edges, the density of states can be approximated by a parabolic band, and α rises with the photon energy as following [13]

$$\alpha h\nu = \mathrm{A}\left(h\nu - E_g\right)^{1/2} \qquad (2.16)$$

where A is constant $\approx \left[\frac{e^2}{nch^2 m_e^*}\right](2\mu^*)^{3/2}$ in which μ^* is the reduced electron and hole effective masses, n is the refractive index, and E_g is the direct band gap with minimum $E_C - E_v$ at the same k value [13].

2.2.1.2 Indirect transition:

In indirect band gap solids, the photon absorption for the photon energies near E_g requires the absorption and emission of phonons during the absorption process, as shown in Fig. 2.4. Absorption corresponds to the energy of photon ($E_g - hv'$), which represents the phonon absorption with energy $\hbar\omega$. For that, α is proportional to $\left[hv' - \left(E_g - hv'\right)\right]^2$. When the photon energy reaches $\left(E_g + hv'\right)$, then the absorption of photon process occurs by phonon emission, for which the coefficient of absorption is larger than that for absorption of phonon [13].

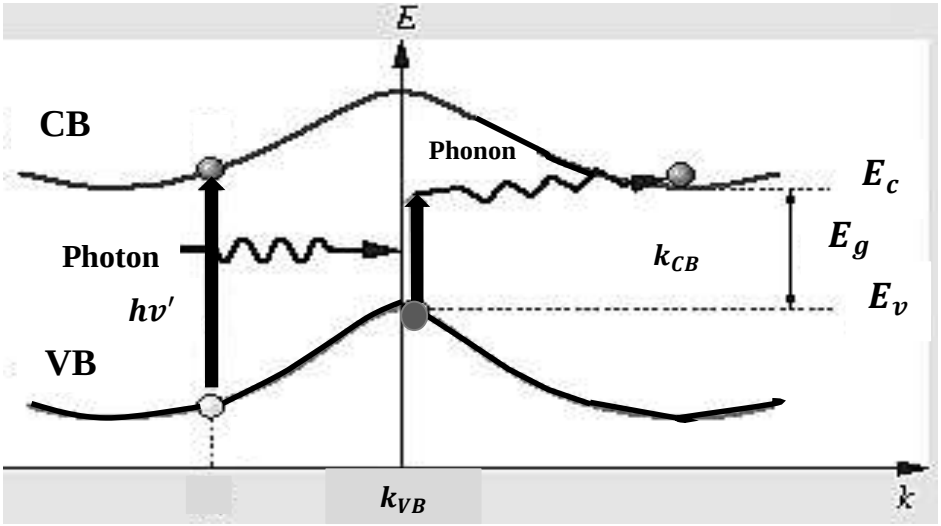

Figure 2.4: An indirect transition across the band gap involve photons.

The absorption coefficient, α, relates to the energy gap E_g through the relation

$$(\alpha E) = B\left(E - E_g\right)^p \qquad (2.17)$$

Where B is a constant depends on the transition probability, E_g is the energy gap and p is an index that characterizes the absorption process.

Then,

P = 2 for indirect allowed transition.

P = ½ for direct allowed transition.

P = 3 for indirect forbidden transition.

P = 1/3 for direct forbidden transition.

The common way to determine the energy gap (E_g) is plotting a graph of $(\alpha E)^{\frac{1}{p}}$ versus photon energy. In suitable value of p is used to obtain linear plot with the widest range of data, the value of E_g will be given by the intercept on the photon energy (E) axes.

2.2.2: Beer- Lambert Law:

The Beer- Lambert law connects the attenuation of light to the properties of the materials through which the light is travelling. Formulated by German mathematician and chemist August Beer in 1852. For each wavelength of light passing through the spectrometer, the intensity of the light passing through the reference cell is measured, referred as I_o. And also, the intensity of the light passing through the sample cell is measured for that wavelength, given symbol I. If I is less than I_o, then the sample absorbed some of the light [14].

The law states that, the absorbance is directly proportional to the concentration in the solution. The relationship can be expressed as:

$$\boldsymbol{A = \epsilon c l} \qquad (2.18)$$

Where A is the absorbance, ϵ is the molar extinction coefficient which depends on the nature of the chemical and wavelength of the light used measured in L mol^{-1} cm^{-1}, c is the concentration of

a given solution in mol L^{-1} and l is the length of the path light must travel in the solution in centimeter.

The above formula is the common form of the Beer- Lambert law, so it can be also written in terms of intensities:

$$A = \log\left(\frac{I}{I_o}\right) = \epsilon c l \qquad (2.19)$$

2.2.3: Absorption band tail (Urbach energy):

The optical absorption spectra of the materials have an essential role as it gives the fundamental information about its composition and its optical band gap. In the optical absorption spectra three main region can be appeared [15], they are:

(1) Weak absorption region, which produce from defects and impurities.

(2) Absorption edge region, which produce due to the perturbation of structural and disorder of the system.

(3) Strong absorption region, that determine optical energy gap.

Along the absorption curve and near the optical band edge there is an exponential part called Urbach tail. This tail appears in low crystalline, the disordered and amorphous materials because these materials have localized states that extended in the band gap. The Urbach rule is given by the following relation:

$$\alpha = \alpha_o \exp\left(\frac{E}{E_e}\right) \qquad (2.20)$$

Where α is the absorption coefficient, α_o is a constant and E_e denotes the energy of the band tail called Urbach energy, which is weakly dependent upon temperature. Taking the logarithm for the two sides of the Eq.(2.20), hence we can get a straight line equation. It is given as follows:

$$\ln \alpha = \ln \alpha_o + \left(\frac{E}{E_o}\right) \qquad (2.21)$$

So then, the energy band tail can be obtained from the slope of the straight line of plotting $\ln \alpha$ versus the incident photon energy (E).

2.3: Impedance Spectroscopy

Impedance spectroscopy is a non-destructive technique, which uses AC signal to excite or perturb a system under investigation and determine the response (voltage or current). Impedance spectroscopy measures the dielectric properties of a medium and impedance as a function of frequency. In addition, we can determine the properties of the surface layers like pore resistance and capacitance [16].

Impedance can be defined as the resistance to flow of an alternating current as it passes through a conducting material. It is also a circuit consists of resistance (R), capacitance (C) and inductance (L), which can be connected in series or parallel.

2.3.1: RLC series Circuit

The RLC series circuit is a single loop circuit with instantaneous current flowing through it; the current for each circuit element have the same value of current. The source voltage V_S drops through each element in circuit of R, L and C with V_R, V_L and V_C, respectively. Here, the voltage will be out of phase with each other. Where V_R is in phase with current, V_L leads the current by 90° and V_C lags the current by 90°. So, V_L and V_C are 180° out of phase and in opposite direction to each other [17]. As shown in Fig. 2.5.

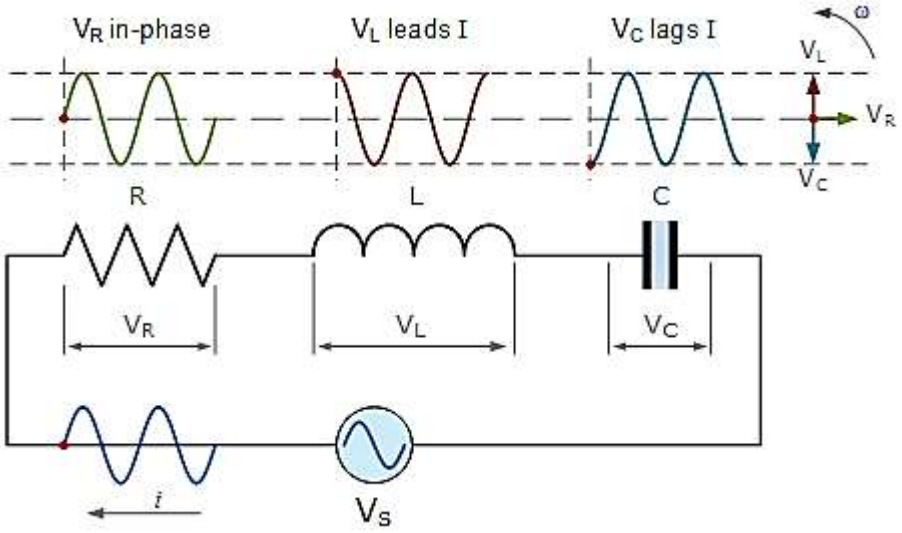

Figure 2.5: RLC series circuit.

In order to get the amplitude of the voltage source V_S, Kirchhoff's voltage law (KVL) will be applied to the RLC series circuit. Which states that around any closed loop, the sum of voltage drops around the loop equals the sum of the electromotive forces (EMF's). After applying the KVL the instantaneous voltage for a series RLC circuit is obtained as:

$$V_s - V_R - V_L - V_C = 0 \qquad (2.22)$$

While the voltage triangle (Fig.2.6) for a RLC series circuit resulted as

$$V_S^2 = V_R^2 + (V_L - V_C)^2 \qquad (2.23)$$

Then,

$$V_S = \sqrt{V_R^2 + (V_L - V_C)^2} \qquad (2.24)$$

Substitute $V_R = I.R, V_L = I.X_L$ and $V_C = I.X_C$ in above equation,

$$V_S = I.\sqrt{R^2 + (X_L - X_C)^2} = I.Z \qquad (2.25)$$

And the impedance will be equal to

$$Z = \sqrt{R^2 + (X_L - X_C)^2} \qquad (2.20)$$

Where I is a current, X_L inductive reactance , X_C capacitive reactance and Z is the total impedance.

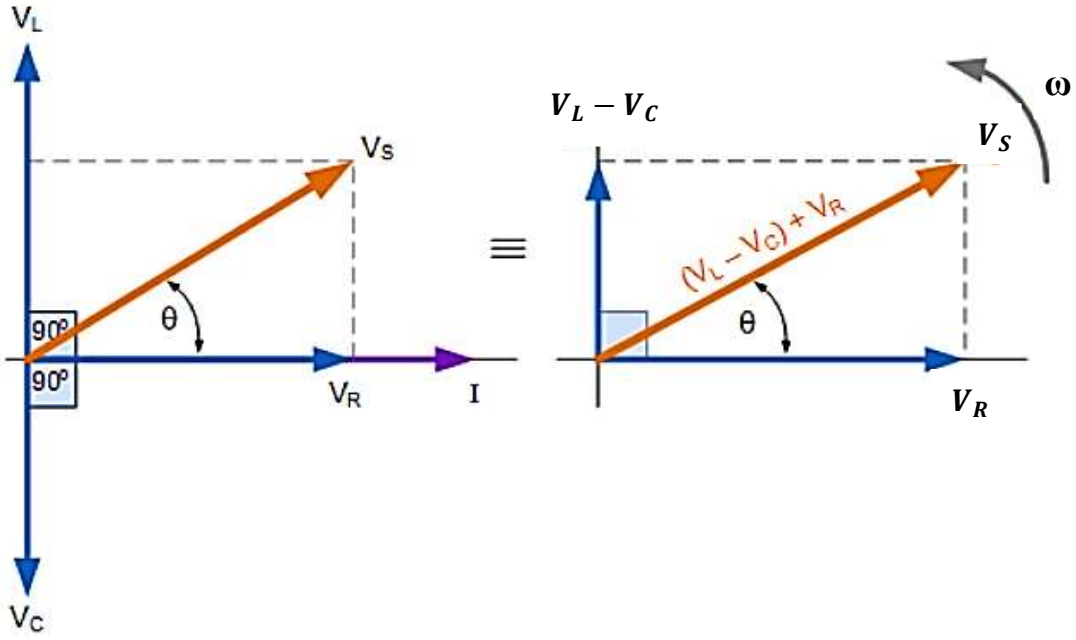

Figure 2.6: Phasor diagram for RLC series circuit.

2.3.2: RLC Parallel Circuit.

In the RLC Parallel Circuit, the applied voltage is now the same for all components of the circuit so we will find the individual branch currents through each element. Which are current flowing through the resister I_R, the current flowing through the inductor I_L and the current flowing through the capacitor I_C [15]. The circuit is presented in Fig. 2.7.

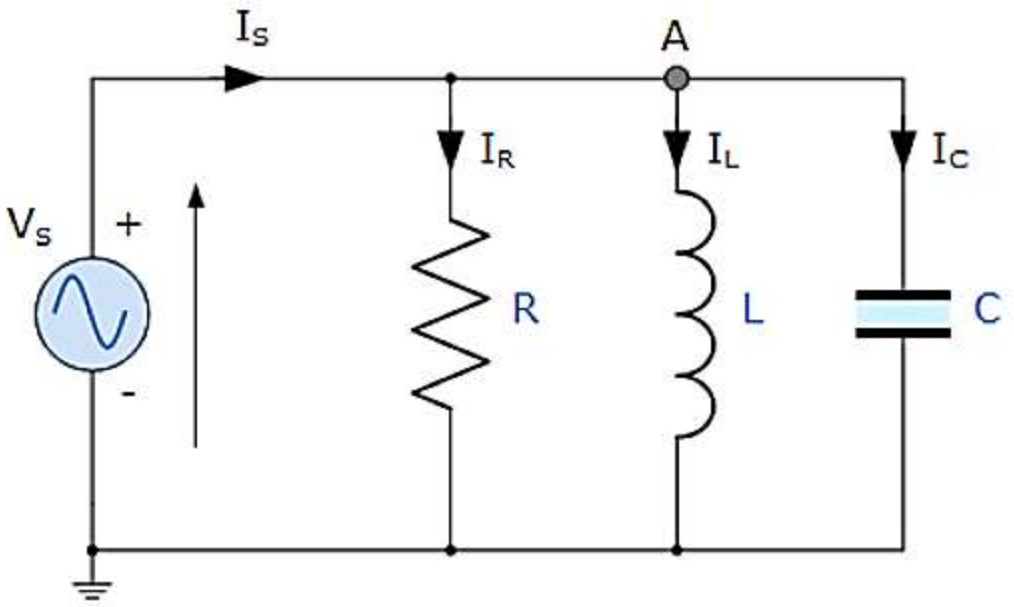

Figure 2.7: The parallel RLC circuit.

So, the current flowing through each branch and therefore each component will be different to each other and also to the supply current I_S. The total current will not be the mathematical sum of each branch currents but their vector sum. Once more time, the current flowing through each branch can be found by using Kirchhoff's voltage law [17].

$$I_S - I_R - I_L - I_C = 0 \qquad (2.26)$$

While the current triangle (Fig.2.7)for RLC parallel circuit is given as follows:

$$I_S^2 = I_R^2 + (I_L - I_C)^2 \qquad (2.27)$$

Then the supply current

$$I_S = \sqrt{I_R^2 + (I_L - I_C)} = \sqrt{\left(\frac{V}{R}\right)^2 + \left(\frac{V}{X_L} - \frac{V}{X_C}\right)^2} = \frac{V}{Z} \qquad (2.28)$$

And impedance Z will be equal to

$$\frac{1}{Z} = \sqrt{\frac{1}{R^2} + \left(\frac{1}{X_L} - \frac{1}{X_C}\right)^2} \qquad (2.29)$$

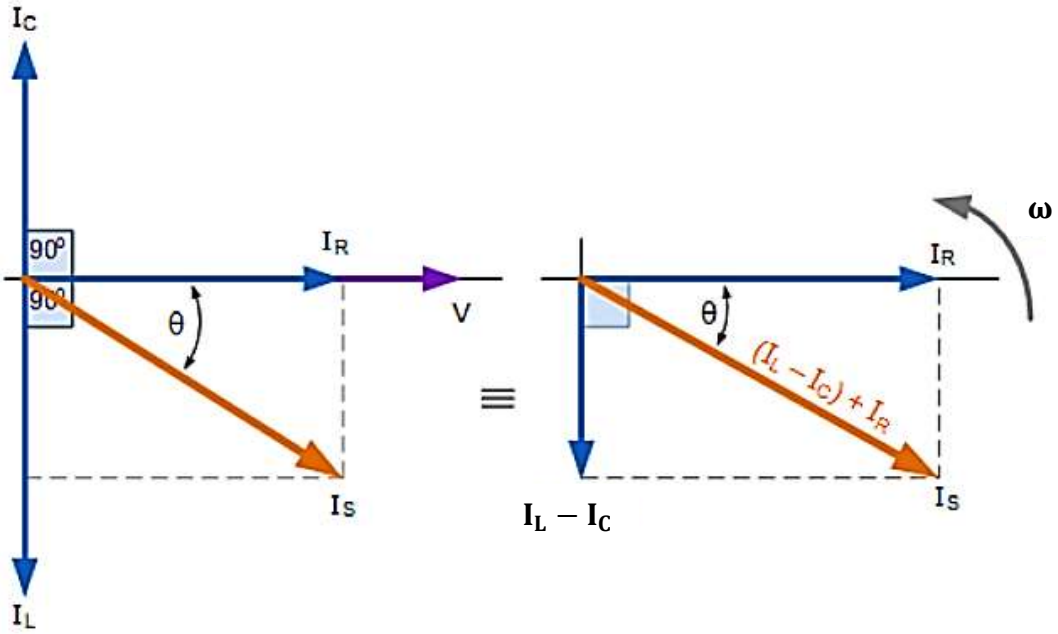

Figure 2.8: Phasor diagram for RLC parallel circuit.

Chapter Three

Experimental Details

3.1: X-ray Diffraction (XRD)measurements:

High purity (98%) Cadmium Bromide ($CdBr_2$) powders were purchased from Alfa Aeser firm.

1. $CdBr_2$ powders are studied by means of X-ray diffraction (XRD) technique in range of (300 -420) K.
2. The powders are in situe heated by using a heat exchanger mounted in X-ray unit and controlled by controller unit shown in figure (3.1).
3. The powders were then left to cool to the room temperature.
4. Samples were also annealed at temperature of 200 ºC, 300 ºC and 400 ºC by using rough vacuum atmosphere.

XRD measured by using Rikago Miniflex 600 diffractometer provided with K_α radiation of a copper anode of wavelength 1.5405 A°, diffraction angles range of 20°-80° at a scanning speed of 1. 2°/ min (see Fig. 3.2). X-ray unit consists of many parts like X-ray tube (source of X-rays), collimator, the sample and a sample holder, the detector, which count the number of X-rays scattered by the sample, and signal processor. "Terror 92" software is used for analysis of the structure of the XRD patterns.

Figure 3.1: Heat exchanger.

Figure 3.2: The Rikago Miniflex 600 diffractometer.

3.2: Optical Measurements

Water is a solvent to $CdBr_2$ due to its high solubility in water. In order to measure the transmittance of the $CdBr_2$ powders, two tubes of quartz which have size of 5.45mL are used as shown in Fig.3.3, The tubes are filled with water, and one of them is used as reference. A 0.1 Molar concentration (M) of $CdBr_2$ powders are added to the second tube, and is shaken for one minute, and then we wait for three minutes in order to precipitate the powders. After that the transmittance is measured in the light incident wavelength ranges of 190 to 1100 nm with the help of UV-VIS-NIR spectrophotometer, which is presented in Fig.3.4. The transmittance is measured at concentrations of 0.2 M, 0.3 M.

Experimental steps:

1. Using the Vision software, choose a rate with 1200 nm/min, band width 2.
2. Put the black bridge inside the UV-VIS spectrophotometer.
3. Record the 100% transmission reference from the command bottom.
4. Hold the two tubes quartz on the sample holder assigned for transmission measurements.
5. Select the T mode and choose the wavelength range of 190-1100 nm.
6. Press on run bottom and collect the data.
7. Repeat step 5 to get sure about the data accuracy.
8. Save the data to be able to analyze the data choose file, then export data as a batch, and then open file by Microsoft excel.
9. Repeat the previous steps for 0.2 M and 0.3 M of CdBr2 powders. And also, for the powders annealed at 200 °C, 300 °C and 400 °C.

Figure 3.3: Quartz tube.

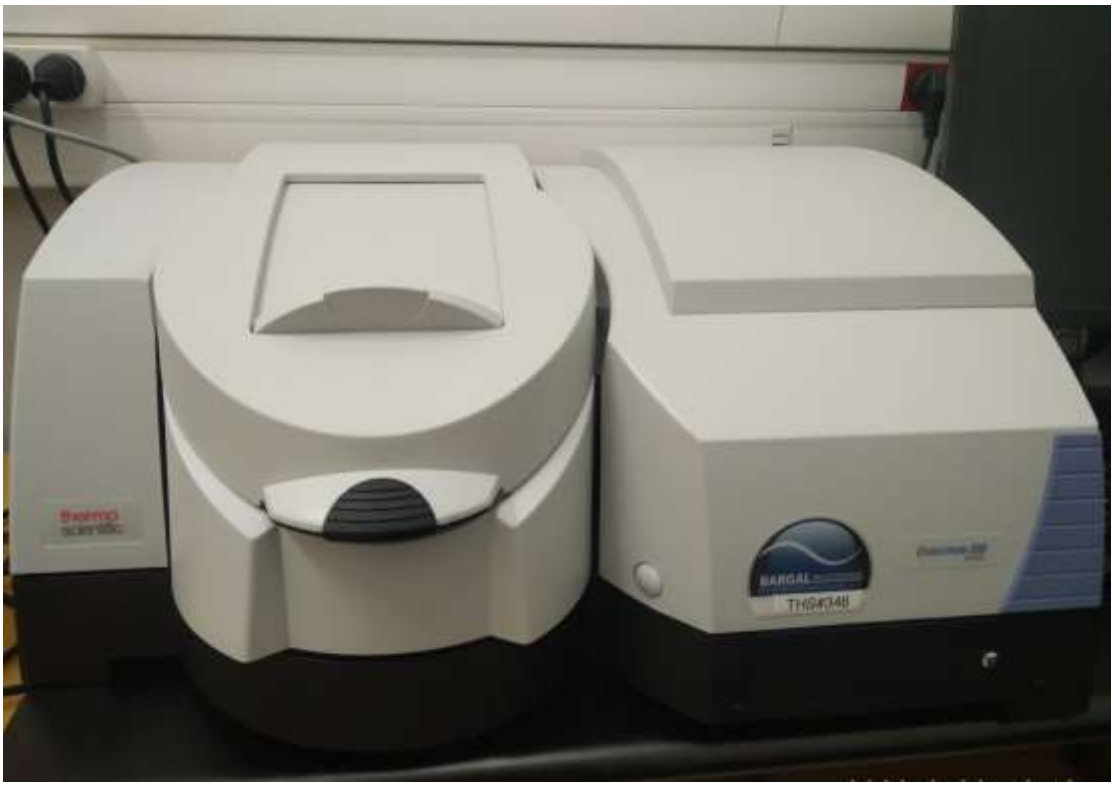

Figure 3.4: The UV-VIS-NR spectrophotometer.

3.3: Current- Voltage (I-V) Measurements.

In order to measure the current values with respect to the voltage for the as grown and annealed $CdBr_2$ powders at 200 °C, 300 °C and 400 °C, all samples were pressed to a pressure of approximately 20 bar with the help of piston to make them like a capsule as shown in Fig. 3.5. The dimensions for as grown and annealed at 200 °C, 300 °C and 400 °C are measured. The diameter size (D) 13.17 mm, 10.45 mm, 10.03 mm and 10.20 mm respectively. The thickness (t) 1.59 mm, 0.85 mm, 0.77 mm and 0.79 mm, respectively. And also, a drop of silver was placed on one side of the capsule and the other side was painted with silver in order to make it conductive so that we could measure the I-V. The Current- Voltage (I-V) measurements were measured at room temperature. In order to determine the electrical resistance of the powders, which were recorded by using Keithley 230 programmable voltage source and Keithley 6481 Pico ammeter. With the help of a MATLab software connected with them by a computer shown in Fig. 3.6.

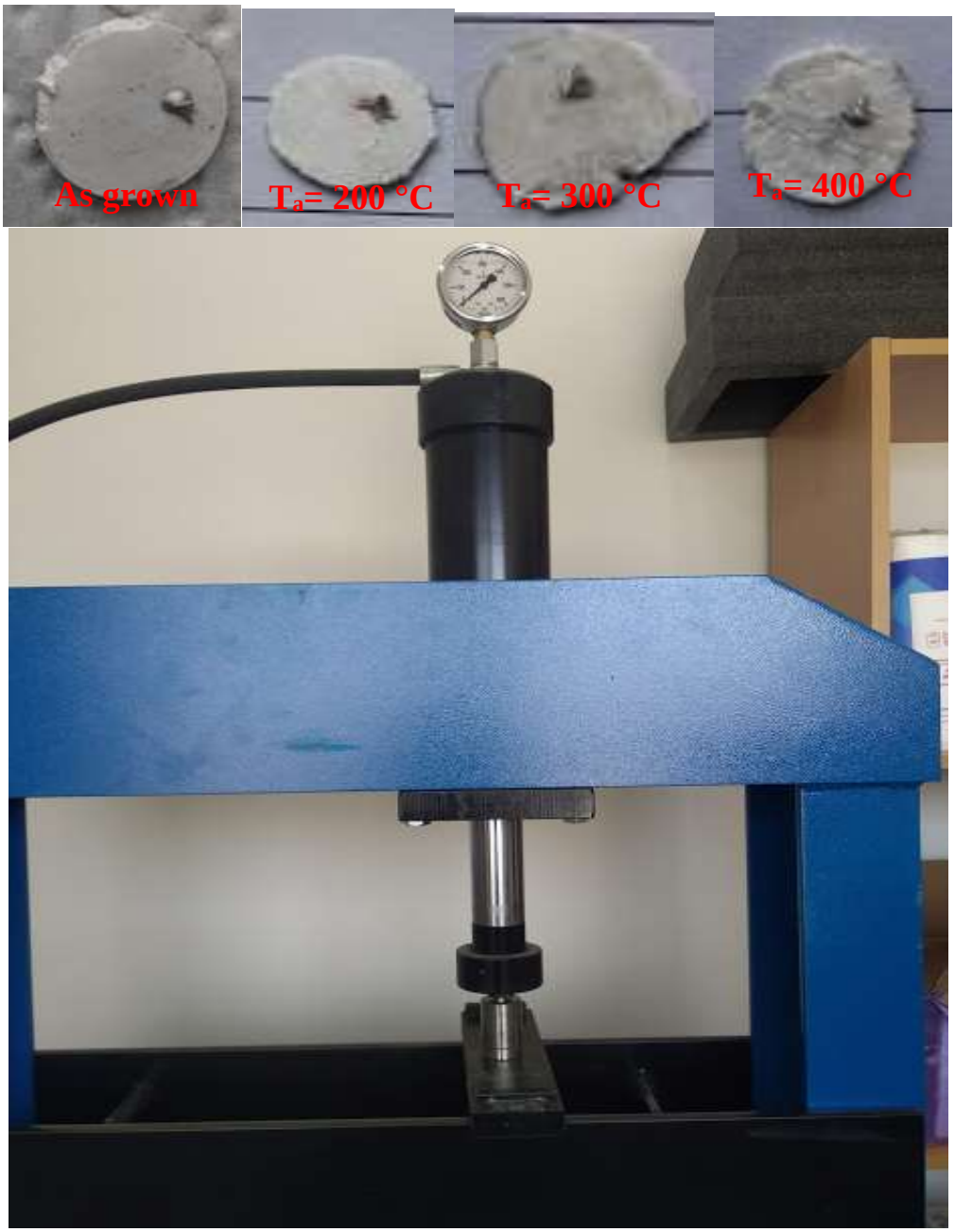

Figure 3.5: Piston and Pressed powders.

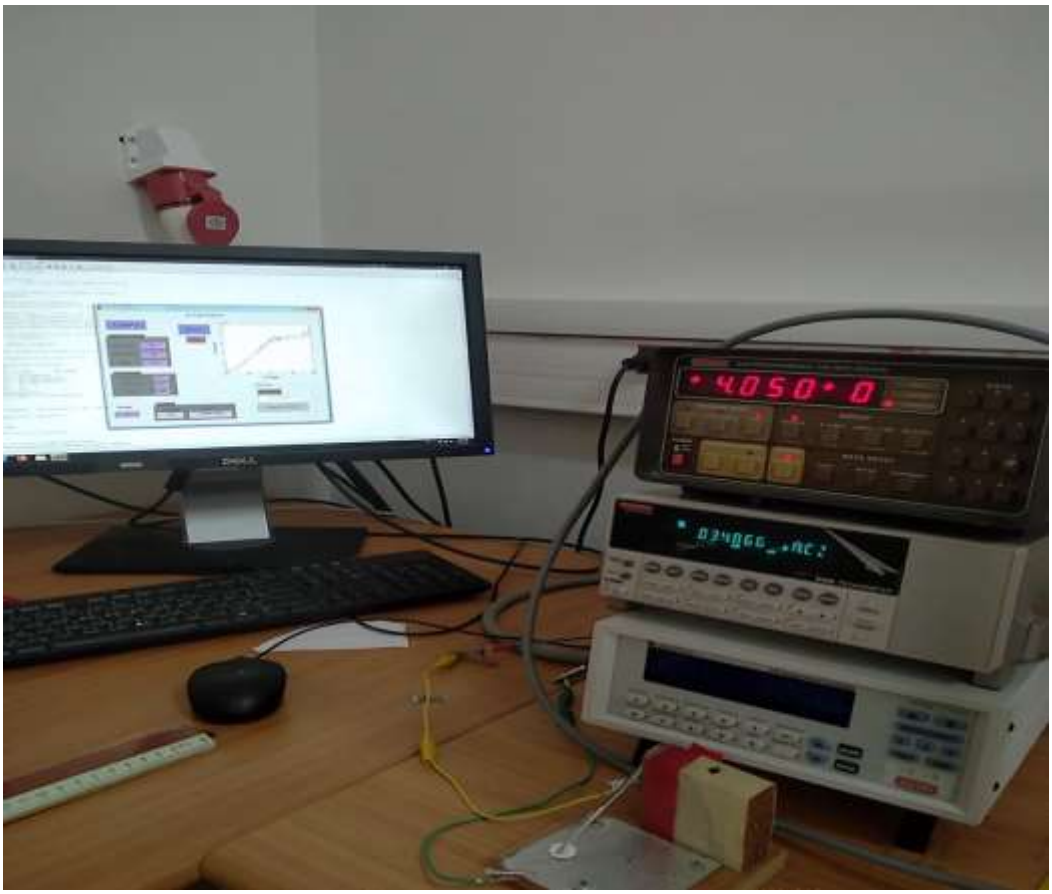

Figure 3.6: IV measurements.

3.4: Impedance Spectroscopy Measurements.

The pressed $CdBr_2$ pure powders and annealed powders at 200°C, 300°C and 400°C were characterized by an impedance analyzer in the frequency range of 10-1800 MHz with the help of Agilent 4291B 10-1800 MHz impedance analyzer (Fig. 3.7) at room temperature. From the impedance analyzer, the impedance (Z), the capacitance on series (C_s), the conductance (G) and the reflection coefficient (ρ) can be measured with the help of MAT Lab software.

Figure 3.7: The impedance analyzer.

Chapter Four

Results and Discussion

4.1: Analysis of the X-ray diffraction technique:

4.1.1: In situe heating process:

The Cadmium bromide powders were purchased from Alfa Aeser firm. The purity of the powders were 98%. The X-ray diffraction (XRD) patterns which resulted from heating the cadmium bromide ($CdBr_2$) powders using a heat exchanger fixed in the XRD diffractometer are shown on Fig.4.1. The heating cycle was in the range of 300-420 K.

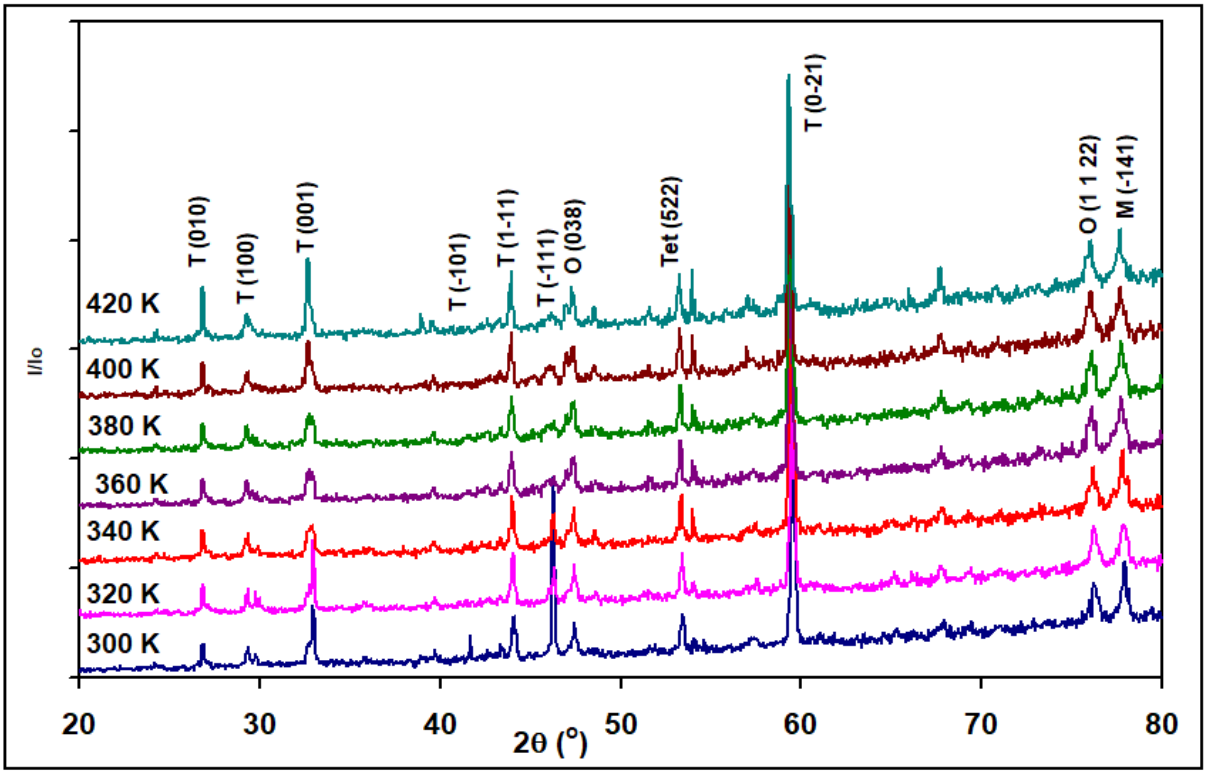

Figure 4.1: The X-ray diffraction patterns for the $CdBr_2$ powders during heating cycles 300 K to 420 K.

The intensive X-ray diffraction patterns are analyzed by the "TREOR 92" software packages. The analysis included all possible structures decisions were taken in accordance with the percentage

differences between the theoretical and the experimentally observed 2θ values. The "TREOR 92" software packages can achieve the Miller indices (hkl) and lattice parameters of specific structure. It can also identify the most appropriate crystal structure. Two methods of solutions were imposed. The first is by entering the observed 2θ values and requesting a solution for particular cell. User can also request the most appropriate lattice parameters. By this method, correctness of solution is tested by comparing the experimentally observed 2θ values and the theoretically calculated ones. 2Δθ differences of less than 0.02 (2%) is accepted as possible solution otherwise it is rejected. The second method of solution require the values of the lattice parameters and the expected unit cell, then it calculates 2θ, (hkl) and intensity values. Operator can then compare experiment with software analysis. "TREOR 92" software packages are intended to give plane orientation and crystal parameters of the observed peaks for all seven possible structures.

Table 4.1 shows the possible structural phases of the $CdBr_2$ powders before heat treatment. The table show the experimentally observed 2θ values for $CdBr_2$ powders at room temperature and intensity. The table also illustrates the values of particular structures percentageΔ2θ %. By taking the smallest difference between all seven structures. It has been found that the powder contains more than one structural phase.

However, the cubic structure was excluded because it didn't not contain all the observed peaks with law error percentage. The difference percentage for the other structures were (0-6.5)% for hexagonal, (0-12.5)% for orthorhombic, (0-8.9)% for tetragonal, (0-6.5)% for trigonal,(0-16.7) % for monoclinic and (0-22.2) % for triclinic. The triclinic structure was found to contain more zeroes diff% values than other structures. So, the first six peaks related to the triclinic structure. Then, we started to compare the diff% between the excluded structures, i.e. the cubic structure for which the smallest value was, so that the peak belonged to the associated structure. After using this method,

it was found that other peaks related to orthorhombic, tetragonal, triclinic and monoclinic. There are no peaks related to the trigonal, hexagonal and cubic structures. The dominant structure is the triclinic which was related to the maximum peak observed at 2θ= 59.55º.

As it resulted from "Treor 92" software data, the powders exhibit triclinic, orthorhombic, monoclinic and tetragonal structure. Our calculation displayed that the phase weight percentages of the triclinic structure is 68.3%.While for the orthorhombic, monoclinic and tetragonal structure is 14.3%, 11.2% and 6.2%, respectively. According to these results, we were back to the "Treor 92" obtained data to get the associated miller indices (hkl) for each peak, see Fig.4.1. In addition, the associated lattice parameters for the maximum peak which is related to triclinic structure a, b, c, α, β and γ are 3.37 Å, 3.72 Å and 2.77 Å, 98.66°, 92.94°, 114.93°, respectively.

Table 4.1: The XRD reflections analysis for the $CdBr_2$ powders before subjected to heat treatment. Possible structural phases are investigated by TREOR 92 software packages.

2θ (Powder)	I (c/s)	I/I_o	Cubic%	Hexagonal%	Ortho.%	Tetragonal%	Trigonal%	Monoclinic%	Triclinic%
26.9	144	10.4		0	0	0	0	0	0
29.4	133	9.6	0	0	0	0	0	0	0
32.95	370	26.6		5.1	0	6.9	5.1	0	0
41.65	215	15.5	41.1	2.7	12.5	4.2	2.7	0	0
44.1	314	22.6		4.2	2.3	8.9	4.2	14.8	0
46.25	1020	73.4		5	6.4	2.2	5	2.4	0
47.45	289	20.8	14	6.5	0.2	5.8	6.5	6.4	21.2
53.45	323	23.3	130.3	5.9	6.2	1.2	5.9	1.2	64
59.55	1389	100.0	144.7	3.5	7.1	5.5	3.5	16.7	0.8
76.3	462	33.3	56.3	4.1	1.1	5.9	4.1	14.2	22.2
77.95	591	42.5		2.5	6.2	3.3	2.5	0.7	3.8

In order to reveal the effect of heating on the $CdBr_2$ powders, the maximum peak which was observed for the triclinic phase in the (0 -2 1) orientation direction were taken into account as the Fig. 4.2 shows the diffraction peaks shifts to the left as the temperature increases. Particularly, the peaks positions shift from $2\theta = 59.55^o$ to 59.3^o. This shift is followed by a decrease in the maximum peak intensity with increasing temperature. As can be seen from the inset of Fig. 4.2, the intensity values fall from 1389 c/s to 1017 c/s as the temperature increase from 300 K to 420 K. In addition, it is also observed that the maximum peak broadens as temperature increases. This behavior of the X-ray patterns indicates the existence of uniform deformation. The deformation which is described by the expansion of bond lengths to the original bonds lengths of the atoms are known as strain.

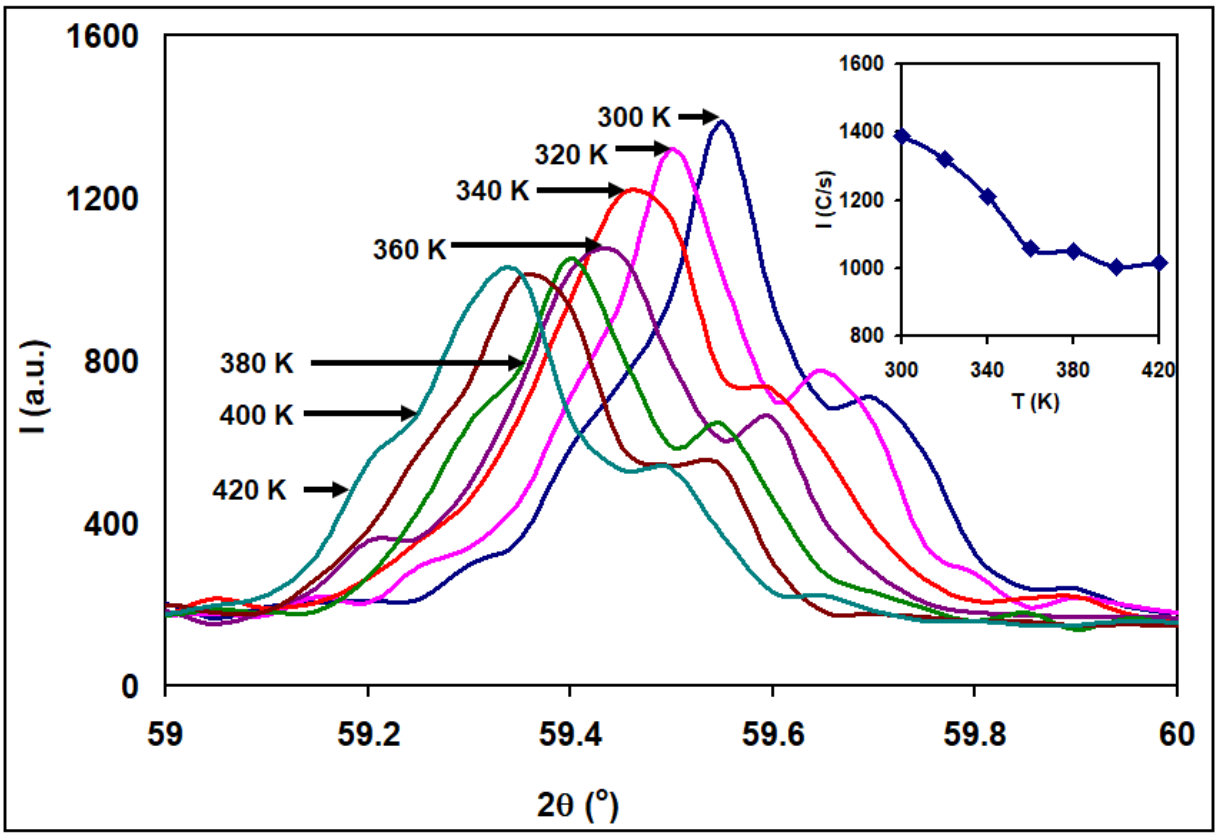

Figure 4.2: The enlargement of the maximum peaks for $CdBr_2$ powder during the in situe heating cycle. The inset shows the variation of the maximum peak intensity with temperature.

Fig. 4.3 (a), (b), (c) and (d) shows a profound effect of heating temperature on some of the structural parameters like crystallite size (D), strain (ε), dislocation density (δ) and stacking faults percentage (SF%). The structural parameters are determined from major peak broadening and 2θ values with the help of the previously mentioned relations (2.8, 2.9 and 2.10). The crystallite size Fig.4.3 (a)) exhibits value of ~63.75 nm at room temperature. It decreased as the temperature increase reaching a value of 51.64 nm at 420 K. On the other hand, as appears in Fig.4.3 (b) lattice strain shows an opposite trend of variation. Namely ε increases with increasing temperature following sharper trend of variation in the low temperature range 300-360 K.

Also, the calculated dislocation density as a function of temperature is shown in Fig. 4.3 (c). Dislocation density exhibits a value of 0.80×10^{14} lines/cm^2 at 300 K. It increased as the temperature increases reaching a value of 1.2×10^{14} lines/cm^2 at 420 K. The same behavior is observed for stacking faults Fig.4.3 (d). Particularly, the stacking faults percentages increases with increasing temperature up to 360 K where it tends to remain constant at higher temperature. The variations of the structural parameters with temperature indicate that the $CdBr_2$ powders exhibit disorder with increasing temperature. The increased structural disorder upon heating in Si was attributed to the formation of doping bonds which results in an increase in the average bond angle variation [20]. It is also possible to think that the crystallite size decreases due to the faster increase of the nucleation rate than the growth rate [21].

When the recrystallization and recovery processes dominates owing to the nucleation mechanisms, small crystallites are consumed to form larger ones. However, as effect density, crystallite size decreases and microstrain increased with increasing temperature, either the recrystallization is incomplete of the minor phases defect dominates [22].

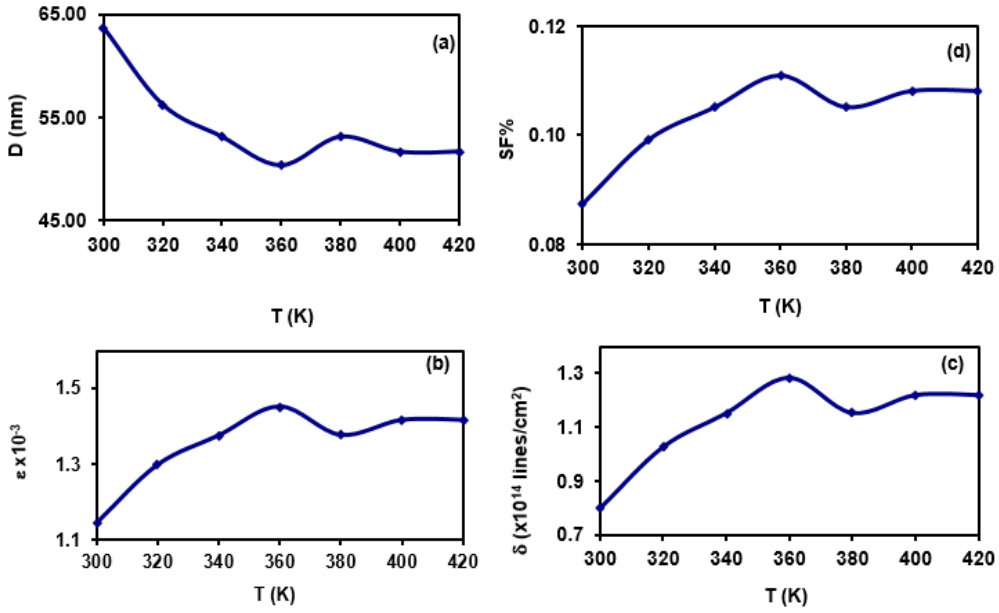

Figure 4.3: Heating temperature effect on the (a) crystal size, (b) strain, (c) dislocation density, and (d) stacking faults.

The X-ray patterns were also measured for the $CdBr_2$ powders before heating to 420 K and after it left to cool to the room temperatures. The XRD patterns are shown in Fig. 4.4. It is clear from the figure that the powders have relaxed to other structural parameters. It is clear from the figure that some of sharp peaks become less intensive and the main peak which is centered at $2\theta = 59.5^{o}$ exhibits higher intensity values. As can be seen from table 4.2 and 4.3, the peak centered at 41.65 ^{o} and 46.25^{o} has disappeared the other sharp peaks are shifted. The XRD patterns (after cooling) are analyzed with the help of "TREOR 92" software packages. The results are tabulated in table 4.2. The analysis shows that the powders after cooling still have the triclinic as major phase, and monoclinic, tetragonal and orthorhombic structures as minor phase. The variation of phases is presented in table 4.3.

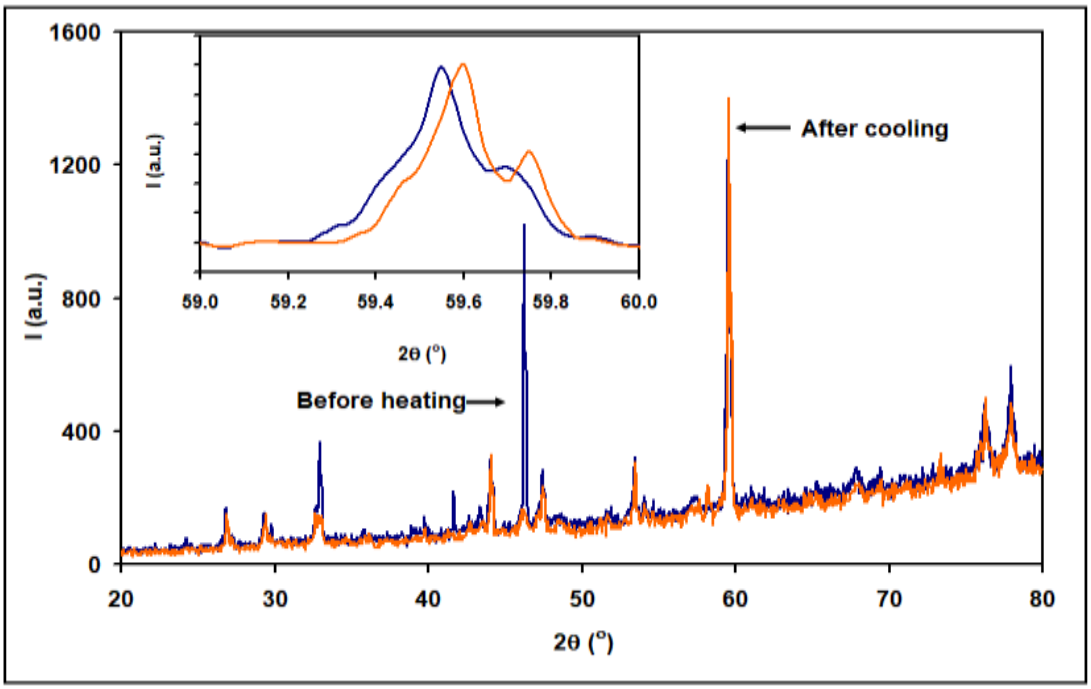

Figure 4.4: X-ray diffraction patterns at room temperature (before heating) and after cooling.

Table 4.2: the XRD reflections analysis for the $CdBr_2$ powders after it left to cool. Possible structural phases are investigated by "TREOR 92" software packages.

2θ (After cooling)	I	I/Io	Cubic%	Hexagonal%	Ortho.%	Tetragonal%	Trigonal%	Monoclinic%	Triclinic%
26.9	152	10.9		0	0	0	0	0	0
29.4	151	10.8	0	0	0	0	0	0	0
33.05	143	10.2		3	0	6	3	0	0
44.1	329	23.5	41.1	4	4.7	4.8	4	0	0
47.1	140	10.0		7.1	2.6	0.8	7.1	23.8	0
47.5	237	16.9		2.1	3.8	3.2	2.1	2.9	0
53.5	308	22.0	14	1.5	1.7	1	1.5	19	17.8
58.2	238	17.0	130	1.7	13	1.2	1.7	1.5	8.2
59.6	1400	100.0	144.7	2.4	3.6	4	2.4	7.4	14.9
76.35	498	35.6	56.3	4.4	0.8	3.7	4.4	14.3	26
77.95	485	34.6		5.6	1.3	0.9	5.6	0.4	22.3

Table 4.3: XRD analysis of $CdBr_2$ powders before heating to 420 K and after it was left to cool.

2θ (Powder)	I	I/I_o	hkl	2θ (After cooling)	I	I/I_o	hkl
26.9	144	10.4	T(0 1 0)	26.9	152	10.9	T(0 1 0)
29.4	133	9.6	T(1 0 0)	29.4	151	10.8	T(1 0 0)
32.95	370	26.6	T(0 0 1)	33.05	143	10.2	T(0 -1 1)
41.65	215	15.5	T(-1 0 1)	44.1	329	23.5	T(1 1 0)
44.1	314	22.6	T(1 -1 1)	47.1	140	10.0	T(0 1 1)
46.25	1020	73.4	T(-1 1 1)	47.5	237	16.9	T(-1 1 1)
47.45	289	20.8	O(0 3 8)	53.5	308	22.0	Tet(1 0 7)
53.45	323	23.3	Tet(5 2 2)	58.2	238	17.0	Tet(3 1 7)
59.55	1389	100.0	T(0 -2 1)	59.6	1400	100.0	H(2 0 13)
76.3	462	33.3	O(1 1 22)	76.35	498	35.6	O(1 2 11)
77.95	591	42.5	M(-1 4 1)	77.95	485	34.6	M(-4 0 1)

The phase weighs which existed in $CdBr_2$ powders before heating and after cooling are calculated in order to reveal the change in the percentages of the phases in the powders. The phase weights are shown in table 4.4. It is clear that there is a significantly changed in the phase weight for every structure before heating and after cooling. Such as tetragonal phases are increased after cooling. On the contrary, phase weight for the triclinic phases significantly decreased after the powders left to cool. Namely, it changes from 68.29% to 28.23%. The orthorhombic phase weight is also decreased. On the other hand, a new phase is appeared after cooling, which is related to the hexagonal structure with phase weight of 34.31%.

Table 4.4: Phase weight for crystal structures for the $CdBr_2$ powders before heating and after cooling to room temperature.

Structure	phase weight%	
	Before heating	After cooling
Triclinic	68.29	28.23
Tetragonal	6.15	13.38
Trigonal	0.00	0.00
Monoclinic	11.26	11.88
Orthorhombic	14.30	12.20
Hexagonal	0.00	34.31
Cubic	0.00	0.00

As shown in the Fig. 4.4, there are peaks whose intensity decreased after cooling, such as at $2\theta = 32.95^o$, 46.25^o and 47.5^o. In addition, a peak of $2\theta = 41.65^o$ disappears after cooling. On the other hand, a maximum peak shifts to the right after cooling. Particularly, the peaks positions shift from $2\theta = 59.55^o$ to 59.60^o. This shift is followed by slight increase in the maximum peak intensity from 1389 to 1400. The maximum peak shift toward to higher angles indicating the contraction of the lattice.

To reveal the variations that occurred for the structural parameter, the crystallite size (D), strain (ε), dislocation density (δ) and stacking faults (SF %) are determined for the maximum peak of the $CdBr_2$ powders before heating where triclinic phase is dominant and after cooling where hexagonal phase dominates. The data is illustrated in the table 4.5. As it is clear from the table that after cooling is associated with larger disorder. Particularly, after cooling deformation is accompanied with smaller crystallite sizes, larger strains, larger dislocation densities and larger stacking faults.

All the calculated structural parameters indicate larger degree of disorder for the after cooling compared to before heating [20,21].

Table 4.5: The structural parameter for $CdBr_2$ powders before heating and after cooling.

Sample	D (nm)	$\varepsilon \times 10^{-3}$	δ ($\times 10^{14}$ lines/cm2)	SF%
Before heating	63.7	1.1	0.79	0.09
After cooling	56.3	1.2	1.02	0.10

4.1.2: Thermal annealing effect.

The thermal annealing was carried out in an oven at vacuum pressure of 1 mbr. The annealing cycle was one hour for each sample. In Fig. 4.5, X-rays diffraction patterns resulting from annealing the $CdBr_2$ powder at different temperature T_a = 25^{o}C, 200 ^{o}C, 300^{o}C and 400^{o}C. In comparison with the un-annealed powders at room temperature, annealing at 200^{o}C and 300^{o}C temperatures resulted in decreased intensity of the maximum peak. However, there are peaks disappeared or became less intensive. Increasing the temperature of annealing to 400℃ resulted additional peaks with increased intensity values.

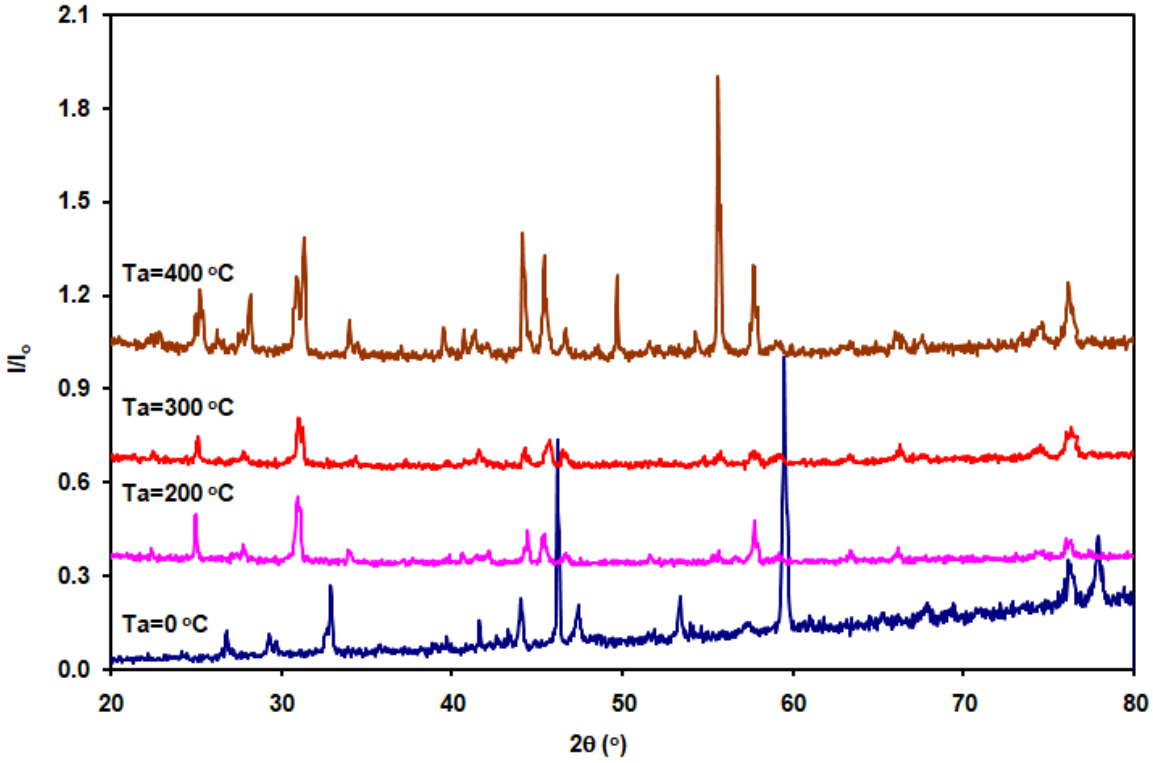

Figure 4.5: X-rays diffraction patterns at different annealing temperatures 200 ^{o}C, 300 ^{o}C and 400 ^{o}C.

The X-ray patterns analyses for the $CdBr_2$ powders which are annealed at 200℃ are tabulated in table 4.6. Thirteen diffraction peaks are observed. The peak analysis which are carried out with the help of "TREOR 92" software packages showed that the annealed powders at 200℃ contain orthorhombic, hexagonal, cubic phases, and also the triclinic phases. The maximum peak appeared at 30.95^{o}. Still the most appropriate solution is the triclinic phase but with the different unit cell parameters. Namely, while the as prepared powders exhibit lattice parameter a= 3.38 Å, b= 3.72 Å, c= 2.77 Å, α= 98.66°,β= 92.94° and γ= 114.94°, the samples annealed at 200℃ reveal cell parameters of a= 5.46Å, b= 4.30 Å, c=3.43 Å, α= 110.03°,β= 93.44° and γ= 100.46°.

Table 4.6: the XRD reflections analysis for the $CdBr_2$ powders at 200 ^oC. Possible structural phases are investigated by "TREOR 92" software packages.

2θ	I	I/I_o	Triclinic %	Ortho. %	Monoclinic %	Tetragonal %	Trigonal %	Hexagonal %	Cubic%
22.5	155	27.3	0	0	0	0	0	0	64.3
25	441	77.8	0	0	0	0	0	0	58.7
27.9	179	31.6	0	0	0	10.8	3.6	3.6	0
30.95	567	100.0	0	21.6	0	7.6	1.1	1.1	7.5
34.15	146	25.7	0	3.5	10.1	9.2	5.1	5.1	26.1
42.2	131	23.1	0	1.1	4.9	3.2	3.1	3.1	0.8
44.45	319	56.3	7.2	0.9	3.1	3.1	6.2	6.2	0.2
45.45	297	52.4	6.1	1.1	10.8	10.8	7.7	7.7	27.5
46.95	118	20.8	27.1	2.2	13.7	9.3	9.4	9.4	34.8
57.8	348	61.4	14.8	1.9	14.8	9.1	22.1	22.1	14.8
63.4	148	26.1	0.3	2.8	3.3	3.4	0.7	0.7	13.5
66.2	176	31.0	10.5	1.4	4.6	2.1	2.6	2.6	16.3
76.25	254	44.8	16.4	6.1	1.5	7.4	0.6	0.6	13.7

The X-ray patterns analysis for the $CdBr_2$ powders annealed 300 ^oC is presented in table 4.7, fourteen diffracted peaks are observed. The repeated analysis showed that the annealed powders at 300 ^oC have triclinic, orthorhombic and hexagonal phases. In addition, a tetragonal phase appeared as new phase. Still the dominant phase is triclinic with the new cell parameters that were obtained at annealing temperature of 300 ^oC.

Table 4.7: The XRD diffraction analyses for the $CdBr_2$ powders at 300 ^oC. Possible structural phases are investigated by "TREOR 92" software packages.

2θ	I	I/I_o	Triclinic%	Ortho.%	Monoclinic%	Tetragonal%	Trigonal%	Cubic%	Hexagonal%
25.15	413	73.2	0	0	0	0	0	0	0
27.9	246	43.6	0	0	0	0	0	122	0
31.05	564	100.0	0	0	0	11.5	0.4	12	0.4
34.45	205	36.3	0	1.9	0	3.1	6.9	16	6.9
41.7	241	42.7	0	11.5	16.9	16.9	4.9	4.8	4.9
44.3	307	54.4	0	0.3	27.7	0.7	0.8	0.8	0.8
45.75	352	62.4	2.8	3.1	7	0.3	1.7	16.1	1.7
46.5	291	51.6	6.2	1.5	1.5	12.2	7.4	34.3	7.4
55.8	237	42.0	4.1	3.1	1.3	1.6	0.2	78.7	0.2
58	237	42.0	34.8	12.6	6.6	1.1	3.7	26.5	3.7
59.5	200	35.5	1.1	7	0.9	0.4	2.7	87	2.7
63.5	225	39.9	10.6	3.8	2.6	0.8	12.3	5.1	12.3
66.3	341	60.5	12	3.8	21.8	0	6.7	14.8	6.7
76.3	438	77.7	7.7	4.7	23.4	2.1	8	28	8

Furthermore, The X-ray patterns analyses for the $CdBr_2$ powders annealed at 400 ^oC are shown in table 4.8.Eighteen diffracted peaks are observed. The analyses of the results showed that there are peaks related to triclinic, orthorhombic, hexagonal and tetragonal. The other peaks are assigned to a new monoclinic phase. For the annealed powders at 400 ^oC the dominant phase is monoclinic with the maximum peak appearing at 55.6^o.

Table 4.8: The XRD diffractions analyses for the $CdBr_2$ powders at 400 ^oC. Possible structural phases are investigated by "TREOR 92" software packages.

2θ	I	I/Io	Triclinic%	Ortho.%	Monoclinic%	Tetragonal%	Cubic%	Trigonal%	Hexagonal%
25.25	544	31.6	0	0	0	0	7.9	0	0
26.25	326	19.0	0	0	0	0	47.5	0	0
28.2	392	22.8	0	0	0	11.2	0	36.2	36.2
31.35	832	48.4	0	14.3	0	12.8	39.4	10.2	10.2
34.05	341	19.8	0	5.1	3.3	5	54.4	2.3	2.3
39.55	335	19.5	0	5	6.6	1	30.8	0.2	0.2
40.75	326	19.0	30.1	13	2.9	6.4	44.5	8	8
41.4	281	16.3		5.5	6.6	3.6	5.4	1.8	1.8
44.15	855	49.7	42.5	5.1	4.3	11.1	19.6	0.2	0.2
45.45	728	42.4	7.5	4.3	0.7	0.9	13.9	4.4	4.4
46.7	293	17.0	3	6.2	5.2	2	44	5.7	5.7
49.7	622	36.2	12.8	1.7	5.9	6	21.6	11.4	11.4
54.3	316	18.4	23.6	3.1	0.8	2.4	7.2	1.6	1.6
55.6	1719	100.0	19.5	5.3	1	1.5	28.7	5.9	5.9
57.75	666	38.7	0.2	2.8	0.7	6.7	56.7	14.2	14.2
66.2	302	17.6	15.2	3.5	3.7	2	18.6	0.6	0.6
74.65	339	19.7	0.7	2.5	0.3	6	3.8	15.2	15.2
76.15	582	33.9	5.2	4.9	7.5	0.4	5.7	4	4

Table 4.9 summarizes the analysis for all annealed samples. Which shows the peaks phases, the *hkl* and also the structure for each peak.

Table 4.9: XRD analysis of annealed $CdBr_2$ powders.

200°C		300°C		400°C	
2θ	hkl	2θ	hkl	2θ	hkl
22.5	T(0 1 0)	25.15	T(0 1 0)	25.25	M(1 0 0)
25	T(0 1 0)	27.9	T(-1 1 0)	26.25	M(0 2 0)
27.9	T(0 0 1)	31.05	T(0 -1 1)	28.2	M(1 0 1)
30.95	T(1 1 0)	34.45	T(-1 0 1)	31.35	M(1 0 2)
34.15	T(1 1 0)	41.7	T(1 0 1)	34.05	T(1 0 1)
42.2	T(-1 1 1)	44.3	T(-1 1 1)	39.55	T(1 -1 1)
44.45	C(4 3 2)	45.75	Tet(4 1 4)	40.75	M(-2 1 15)
45.45	O(3 0 5)	46.5	O(0 4 0)	41.4	Trig(0 0 11)
46.95	O(3 1 5)	55.8	Trig(6 6 1)	44.15	Trig(2 2 1)
57.8	O(1 1 11)	58	Tet(6 1 3)	45.45	M(0 0 12)
63.4	T(-1 -2 2)	59.5	Tet(6 3 0)	46.7	Tet(3 3 0)
66.2	O(0 3 11)	63.5	Tet(6 2 4)	49.7	O(3 3 1)
76.25	Trig(9 0 4)	66.3	Tet(6 4 2)	54.3	M(-2 3 13)
		76.3	Tet(4 0 9)	55.6	M(-3 0 10)
				57.75	T(4 -1 1)
				66.2	Trig(0 0 17)
				74.65	M(-1320)
				76.15	Tet(3 2 16)

The phase weight for the annealed powders is also determined to figure out the variation that occurred in the crystal structure after annealing process. As listed in table 4.10, the annealing significantly affected on the phase weight of crystal structures. Particularly, the phase weight for triclinic structure is decreased with annealing from 68.3% to 13.7%. For tetragonal structure the phase weight in T_a=25 ^oC is 6.15%, then when T_a=200 ^oC it is disappeared, and at T_a=300 ^oC, the phase weight is strongly increased and reach value of 41.7%, and then at T_a = 400 ^oC it is decreased to reach value of 8.9%. The phase weight for hexagonal structure is increased with annealing from 0% to reach value of 14.7% at annealing temperature of 25 ^oC and 400 ^oC. Moreover, for the monoclinic structure the phase weight at T_a= 25 ^oC is 11.3%, then at T_a= 200 ^oC and T_a= 300 ^oC the monoclinic structure disappeared. At T_a = 400 ^oC it is significantly increased reaching value of 56.4%.

The above results indicate that there is a phase transition occurred when the annealed temperature increases, the phase transition change from triclinic to monoclinic phase.

Table 4.10: Phase weight for the $CdBr_2$ powders annealed at 0 °C, 200 °C,300 °C and 400 °C.

Structure	(Phase weight %)			
	Ta= 25 ^oC	Ta = 200 ^oC	Ta = 300 ^oC	Ta= 400 ^oC
Monoclinic	11.3	0	0	56.4
Triclinic	68.3	53.9	46	13.7
Cubic	0	9.7	0	0
Orthorhombic	14.3	28.6	6.8	6.3
Trigonal	0	0	0	0
Tetragonal	6.15	0	41.7	8.9
Hexagonal	0	7.7	5.5	14.7

To reveal the profound effect of annealing on the structural parameters, the crystallite size (D), strain (ε), dislocation density (δ) and stacking faults (SF %) are calculated for the major peak for all annealed powders. As shown in the table 4.11.

Table 4.11: structural parameters for the $CdBr_2$ powders annealed at 0°C, 200°C,300°C and 400°C.

Sample	a (Å)	b (Å)	c (Å)	α (°)	β (°)	γ (°)	D (nm)	ε ($\times 10^{-3}$)	δ ($\times 10^{14}$ lines/cm^2)	SF%
T_a= 0 °C	3.38	3.72	2.77	98.66	92.94	114.94	63.7	1.1	0.80	0.09
T_a=200°C	5.46	4.30	3.43	110.03	93.44	100.46	25.3	5.4	5.8	0.29
T_a=300°C	3.98	4.00	3.27	108.67	93.67	108.63	19.6	6.9	13.3	0.37
T_a=400°C	5.32	6.78	36.09	90.00	138.49	90.00	66.5	1.2	0.50	0.09

It is clear from the table that annealing at T_a = 400 ^oC increased the crystallites size or to sufficiently large values. The annealing at 400 ^oC also lowered the defect density leading to an enhanced structure [20]. The lower defect density that was achieved via annealing is ascribed to the disappearance of a kind of lattice defect different from [21] a point defect. It also indicates the formation of amorphous islands and point defects at different positions [21].

4.2: Optical properties:

In order to explore the heat treatments effects on the optical properties, the transmittance spectra were recorded. The spectra were recorded in the range of 190-1100 nm. The transmittance spectra for $CdBr_2$ aqueous solutions of various concentrations are shown in Fig. 4.6. It is clear from the figure that the transmittance displays maxima (%T) in ultraviolet range (252-400 nm). The higher the concentration is, the more transparent the solution is. Particularly, the transmittance maxima

with a wavelength of 290 nm increases from 30.39% for 0.1 M to 32.51% for 0.2 M and reaches to 35.53% for 0.3 M. It can be also seen from Fig. 4.6 that there is an obvious shoulder beside the maxima peak. The position of the shoulder is located at 400 nm, the transmittance for the shoulder is also increased with increasing molar concentrations. It is actually increasing from 26.32% for 0.1 M, to 28.38% for 0.2 M, and reaches 32.78% for 0.3 M. In the visible light (400-750 nm) and infrared light ranges the transmittance decreased reaching value of 16.7% for 0.1 M, 19% for 0.2 M, and then 23.2 for 0.3 M at 940 nm.

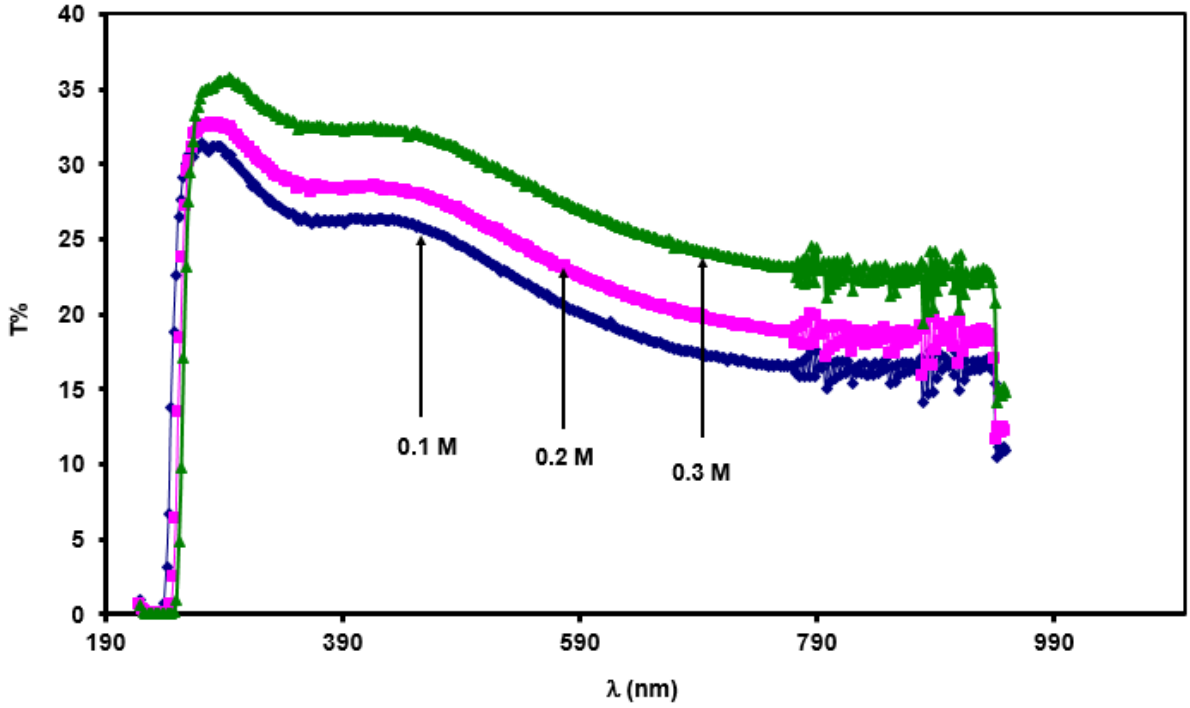

Figure 4.6: The transmittance spectra for the $CdBr_2$ powders at different concentrations 0.1M,0.2M and 0.3 M.

The transmittance spectra were also measured for the $CdBr_2$ powders annealed at 200 °C for different concentrations. It is presented in Fig. 4.7. As can be seen from the figure, as the concentration increases the transmittance maxima also increases. Particularly, the value of transmittance maxima with wavelengths of 278 nm increased from 21.76% for 0.1 M, to 24.46 %

for 0.2 M, and reaches 25.63% for 0.3 M. From figure 4.7, it can be also noticed that there is a shoulder appeared at 350 nm. The transmittance values increase from 19.71 % for 0.1 M, then reach a value of 22.53% for 0.2 M, reaches 24.41% for 0.3 M. In the visible light region, the transmittance decreased.

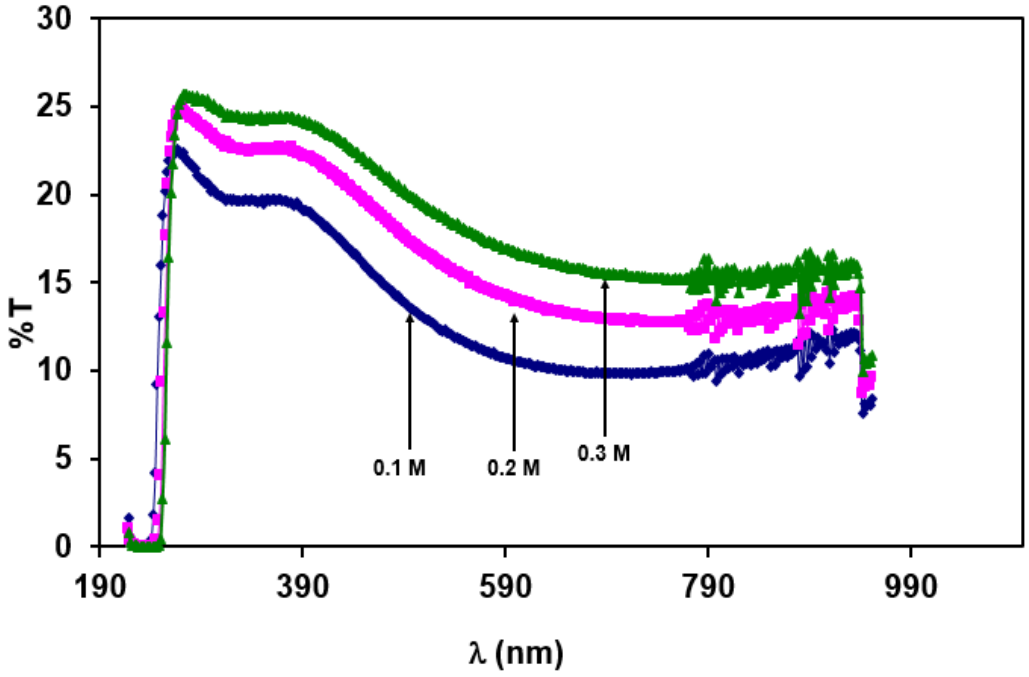

Figure 4.7: The transmittance spectra for the $CdBr_2$ powders annealed at 200 °C for different concentrations 0.1M, 0.2M and 0.3 M.

The transmittance as a function of a wavelength was measured for the powders annealed at 300 ^oC for different concentration. It is shown in Fig. 4.8. The transmittance maxima increases followed by increasing FWHM with increasing the concentration. It is varied from 8.66%, to 14.42%, and 15.07% at 0.1 M, 0.2 M and 0.3 M respectively. There is no a shoulder appeared for the $CdBr_2$ powders annealed at 300 °C in the transmittance spectra. In contrast to what was observed for as prepared and samples annealed at 200 ^oC, in the visible light region, the transmittance spectra displayed and increasing trend of variations.

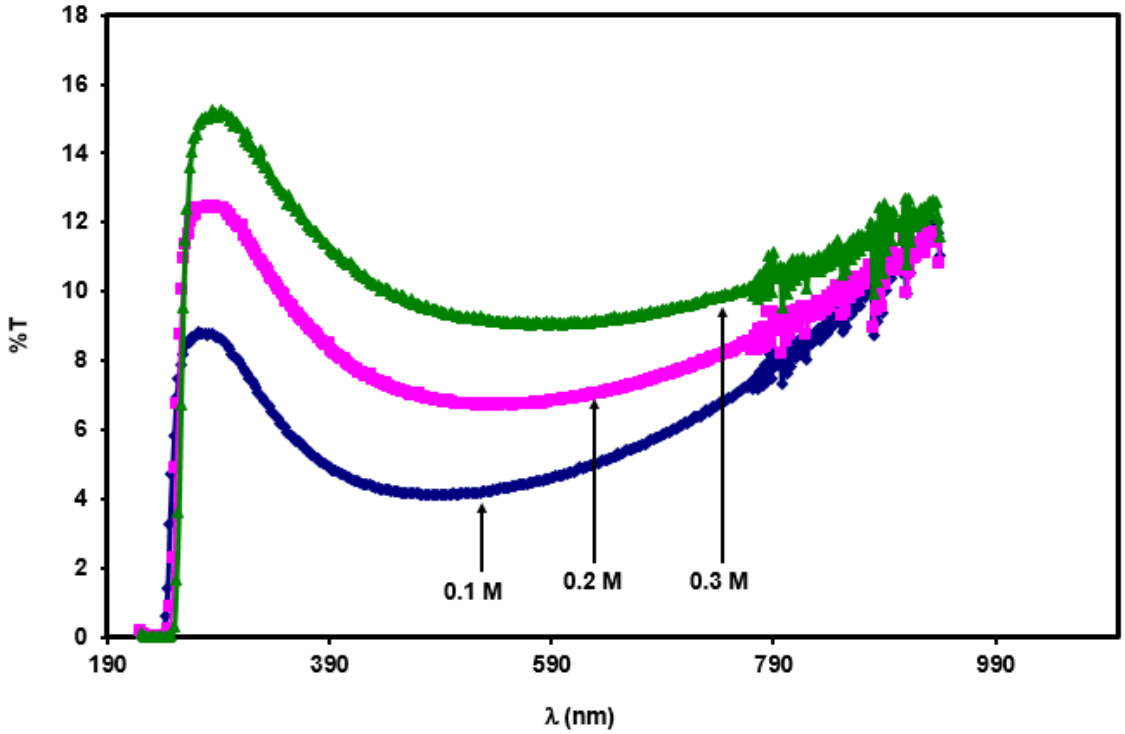

Figure 4.8: The transmittance spectra for the $CdBr_2$ powders annealed at 300 ^oC for different concentrations 0.1 M, 0.2 M and 0.3 M.

In addition, the transmittance spectra for $CdBr_2$ powders annealed at 400 ^oC are measured for various concentrations and presented in Fig. 4.9. The transmittance maxima with a wavelength of 270 nm is increased from 4.32% for 0.1 M, to reaches value of 18.68% for 0.2 M, and then exhibit value of 14.80% for 0.3 M. The full width maxima (FWHM) is also increased as the concentration increased. There is no a shoulder appeared for the $CdBr_2$ powders annealed at 400 ^oC in the transmittance spectra. Above 400 nm, T% values also increased.

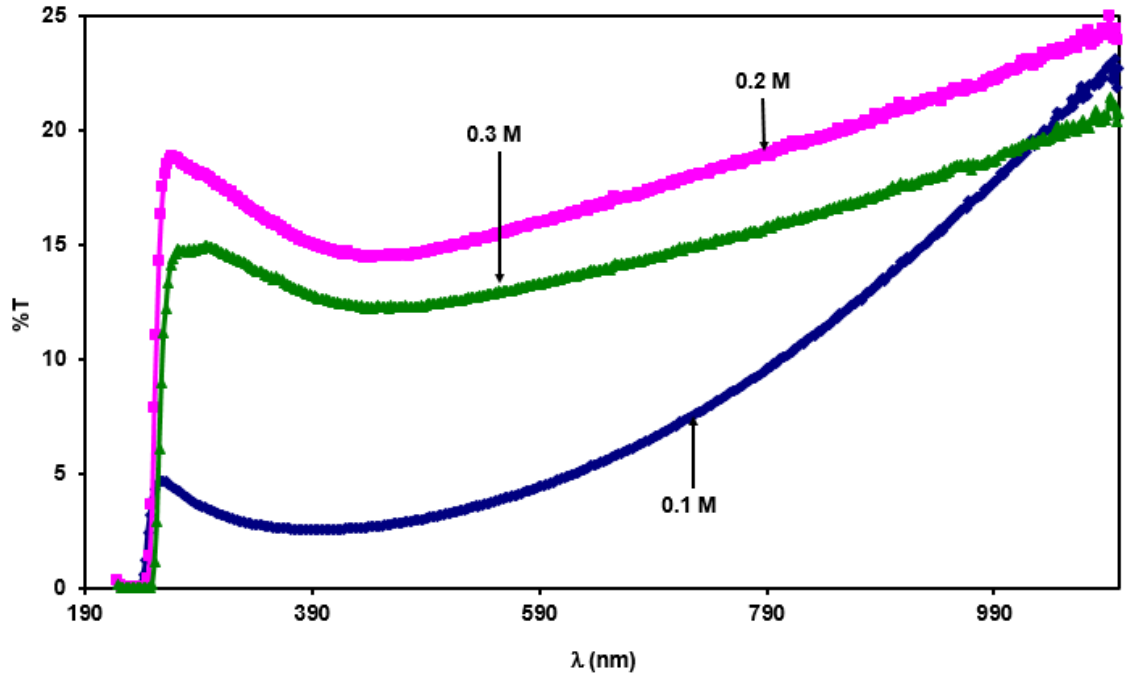

Figure 4.9: The transmittance spectra for the $CdBr_2$ powders annealed at 400 C for different concentrations 0.1 M, 0.2 M and 0.3 M.

We consider the concentration of 0.1 M for all annealed samples to show the effect of annealing of the transmittance spectra. As shown in Fig. 4.10, the maximum transmittance is remarkably decreased with increasing the annealing temperature. Particularly, the maximum transmittance values for annealed powders at 25 ^{o}C, 200 ^{o}C, 300 ^{o}C and 400 ^{o}C are 31%, 22.3%, 8.7% and 4.3%, respectively, at wavelength of 270 nm.

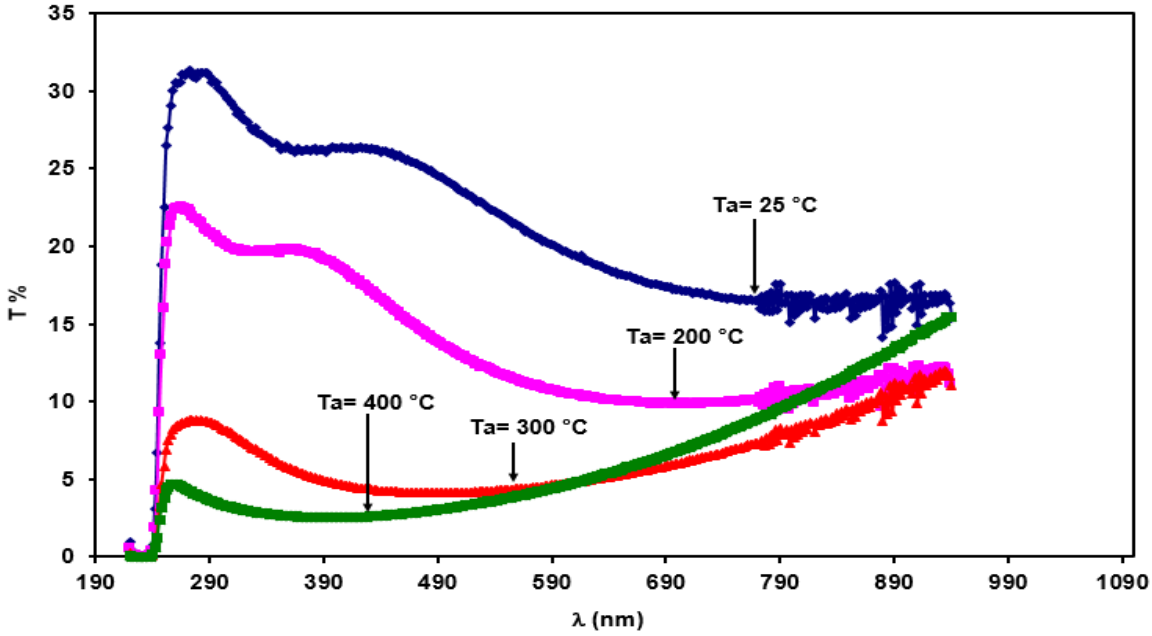

Figure 4.10: The effect of annealing of the transmittance spectra at concentration of 0.1 M for all annealed samples.

The measured transmittance spectra for the $CdBr_2$ annealed powders at concentration of 0.1 M are used to determine the absorbance (A) spectra through the relation ($A = -\log\left(\frac{1}{T}\right)$). The absorbance as a function of incident energy are shown in Fig. 4.11. The figure shows that there is a shift to the left on the absorption maxima, and also this shift is followed by an increase of the maxima absorbance values with increasing the annealing temperatures. The higher the annealed temperature, the higher the absorbance value. The increase in the absorbance values with increasing annealed temperatures may be assigned to the direct allowed transition [23]. The energy band gaps for annealed samples can be calculated from Tauc's equation. The values of energy band gap are 5.10 eV, 5.0 eV, 4.98 eV and 4.90 eV for annealed samples at T_a= 25 °C, 200 °C, 300 °C and 400 °C, respectively. From the values of energy band gaps, it can be noticed that the values decreased with increasing annealed temperature. The decrease of energy band gap values with increasing annealed temperature was ascribed to the creation of bonds around the surface of

crystallites at the time of crystallization growth while changing the structure as observed by XRD. Because of these bonds, defects are produced. As the quantity of defects and bonds with annealing temperature is enhances, the concentration of localized states also increased in band gap [24]. Therefore, the increasing the annealing temperature causes an expansion of width of localized states leading to the decrease in the energy band gap.

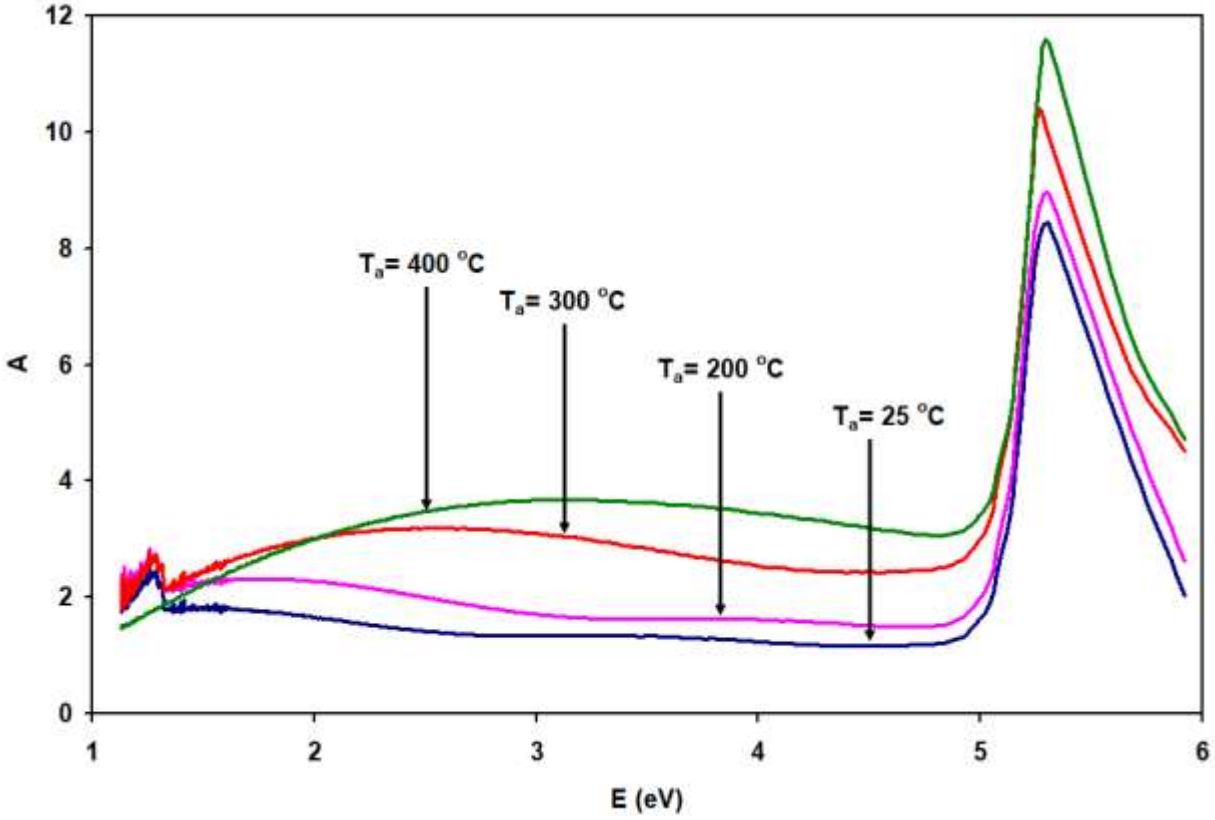

Figure 4.11: The effect of annealing of the absorbance spectra at concentration of 0.1 M for all annealed samples.

The measured transmittance spectra for the $CdBr_2$ powders are used to determine the absorbance (A) spectra through the relation ($A = -\log\left(\frac{1}{T}\right)$) , the absorbance as a function of incident energy are shown in Fig. 4.12. As can be seen from the figure, that the absorbance maxima increasing and the FWHM become broaden as the concentration increases. The values of absorbance maxima

increased from 8.9 for 0.1 M, to 9.5 for 0.2 M and to 9.6 for 0.3 M. From the absorbance spectra, information about the energy gap can be revealed for $CdBr_2$ powders. The optical energy gap for the direct allowed transitions is determined from the absorbance by applying Tauc's relations, it is shown in Fig. 4.13. Which are 5.11 eV, 5.00 eV and 4.92 eV for concentrations of 0.1 M, 0.2 M and 0.3 M. The values of energy band gaps decreasing as the concentration increased. The band gaps become narrower.

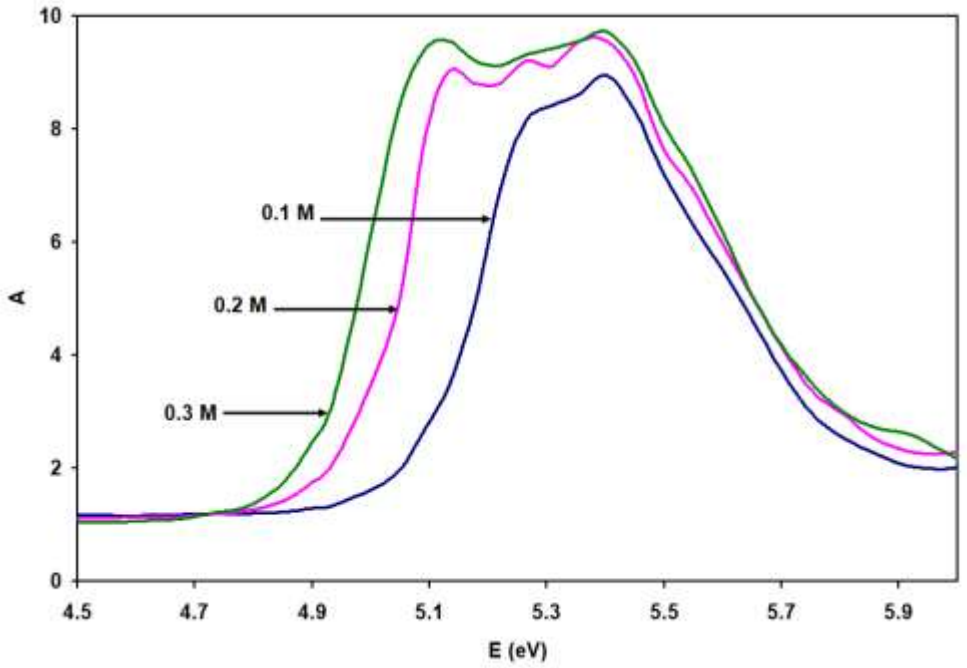

Figure 4.12: The absorbance spectra for the $CdBr_2$ powders at different concentration 0.1 M, 0.2 M, 0.3 M.

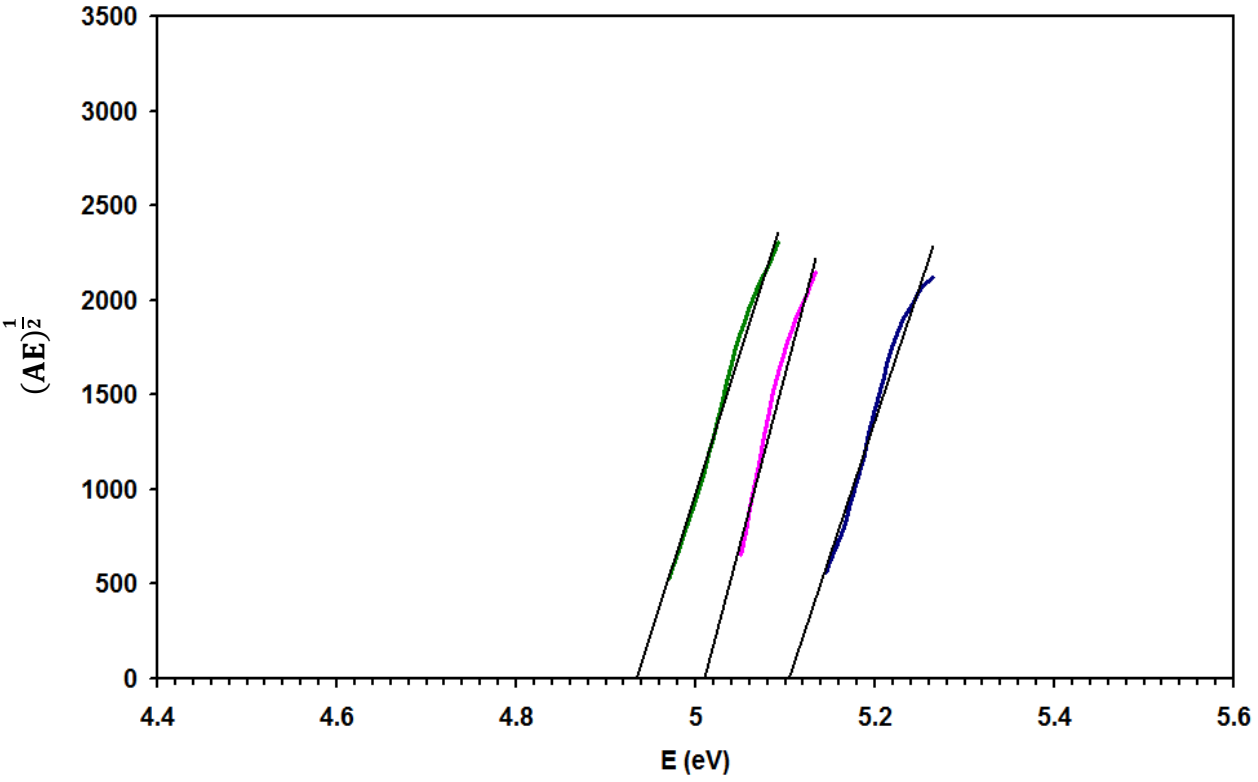

Figure 4.13: The Tauc's equation representative fittings for the $CdBr_2$ powders.

The absorbance spectra for $CdBr_2$ powders annealed at 200 ^oC are shown in Fig. 4.14. As can be seen, that the absorbance maxima are increased and it broadens as the concentration increase. The values of the absorbance maxima are observed, at the concentration of 0.1 M it is 9.6, for 0.2 M it is 10, and for 0.3 M it is 10.8. The optical energy gaps for the direct allowed transition are determined. Which are 5.10 eV, 4.95 eV and 4.87 eV for concentration of 0.1 M, 0.2 M and 0.3 M, respectively. The values of energy gaps are slightly decreased by increasing the concentration of the annealed powders at 200 °C. A band gap became narrower.

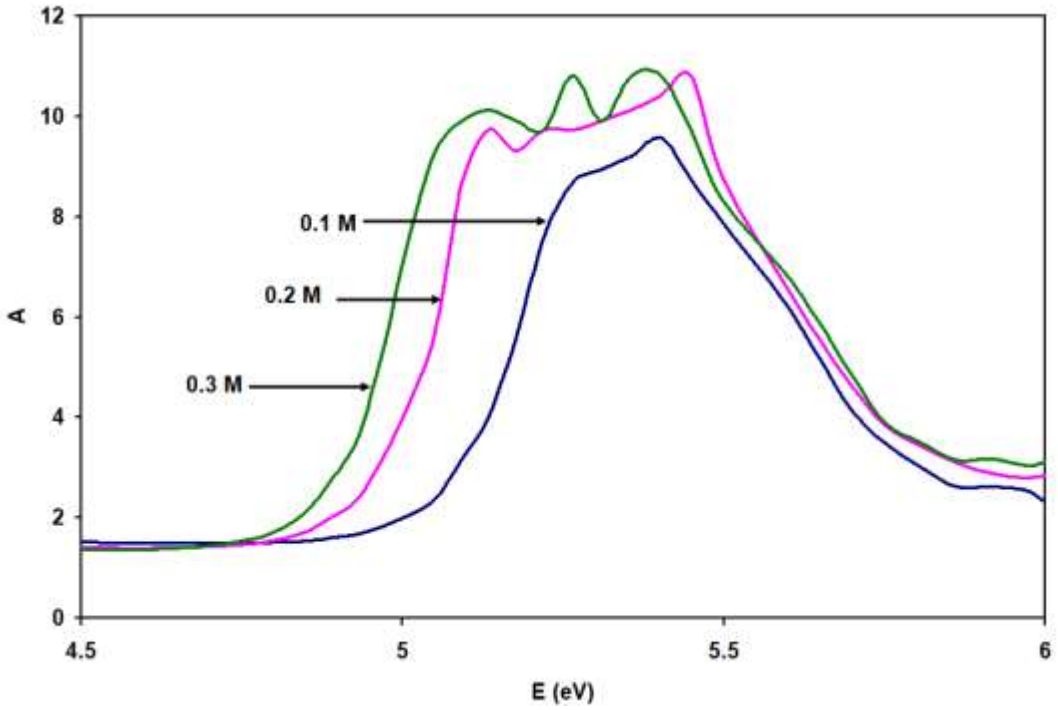

Figure 4.14: The absorbance spectra for the $CdBr_2$ annealed at 200 °C powders at different concentration 0.1 M, 0.2 M, 0.3 M.

In addition, the absorbance is determined for the annealed $CdBr_2$ powders at 300 °C which are shown in Fig. 4.15. Three regions appeared in the absorption spectra. These regions are the sharp region above 4.9 eV, absorption saturation region between 4.9-3.3 eV, and transparent region below 3.3 eV. In the sharp region, the absorbance values are decreased and the curves shifted to the left as the concentration is increased. Also, from the figure can be noticed that the absorbance values don't reach zero in the transparent region. This indicates the presence of band tails. The band tails are usually formed by impurities, defects and broken bonds. As the figure shows that increasing the concentration of annealed powders at 300 °C causing lower degree of absorption. In the low absorption region, where the band tails are existed, the energy band tails can be determined from the reciprocal of linear slope of ln (A) – E changes which are presented in Fig.4.16 (a). The energy band tails indicate the presence of defects in the structural and optical

transition between the localized and extended state in the valence and conduction bands [17]. The estimated values of the band tails energy are 2.02 eV, 2.69 eV and 4.74 eV for concentration of 0.1 M, 0.2 M and 0.3 M, respectively. Energy band gaps for annealed powders at 300 °Care observed. The values of energy gaps for the direct allowed transition are 5.00 eV, 4.90 eV and 4.81 eV for concentration of 0.1 M, 0.2 M and 0.3 M, respectively. As can be noticed, that the values of energy gaps decreased as the concentration increased. A band gap became narrower.

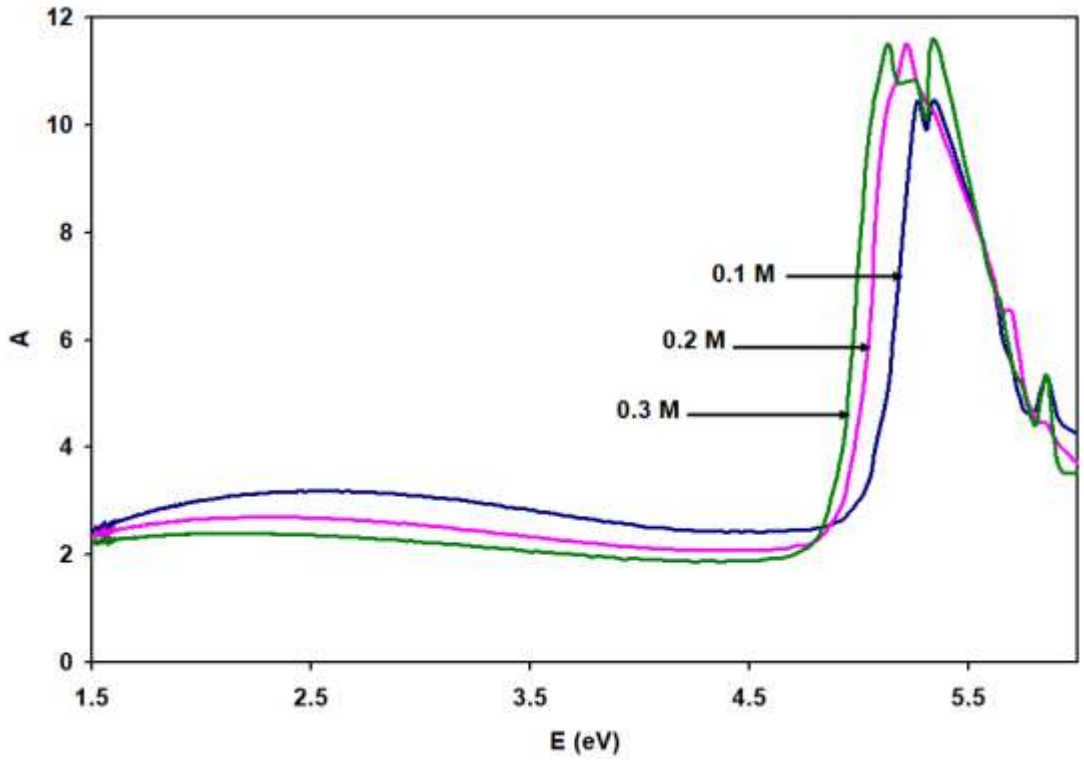

Figure 4.15: The absorption coefficient spectra for the $CdBr_2$ annealed at 300 °C powders at different concentration 0.1 M, 0.2 M, 0.3 M.

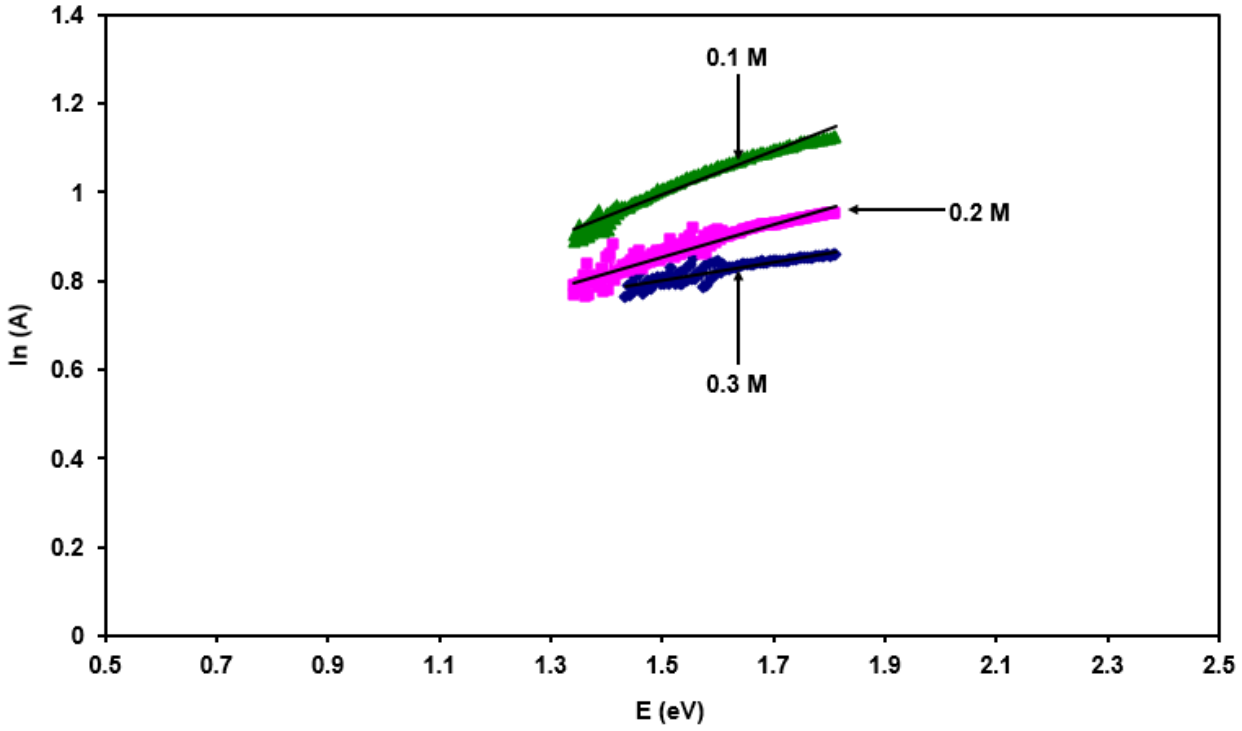

Figure 16: The ln(A)$-E$ variations for $CdBr_2$ powders annealed at 300 °C for different concentration.

Moreover, the absorbance as a function of energy for the $CdBr_2$ powders annealed at 400 °C are displayed in Fig. 4.17. Three regions appeared. These regions are the sharp region above 4.8 eV, the absorption saturation region between 4.8-2.5 eV and the transparent region below 2.5 eV. In the sharp region the A values are shifted to the left as the concentration is increased. In the absorption saturation region, the absorbance become constant due to the filling of the conduction band by electrons. Also can be seen, that the values of absorbance don't reach zero. This indicates to presence of band tails related to presence of impurities, defects and broken bonds [17]. In the low absorption region, where the band tails are existed, the energy band tails (E_e) can be determined from the reciprocal of linear slope of ln (A) – E changes which are presented in Fig. 4.18. The calculated E_e are 0.96 eV, 2.29 eV and 2.50 eV. The optical band gaps for the annealed powders at 400 °C are calculated. The values of energy gaps for the direct allowed transition are

5.10 eV, 4.91 eV and 4.85 eV for different concentrations. It can be noticed that the band gap became narrower with increasing the concentration of the annealed powders at 400 °C.

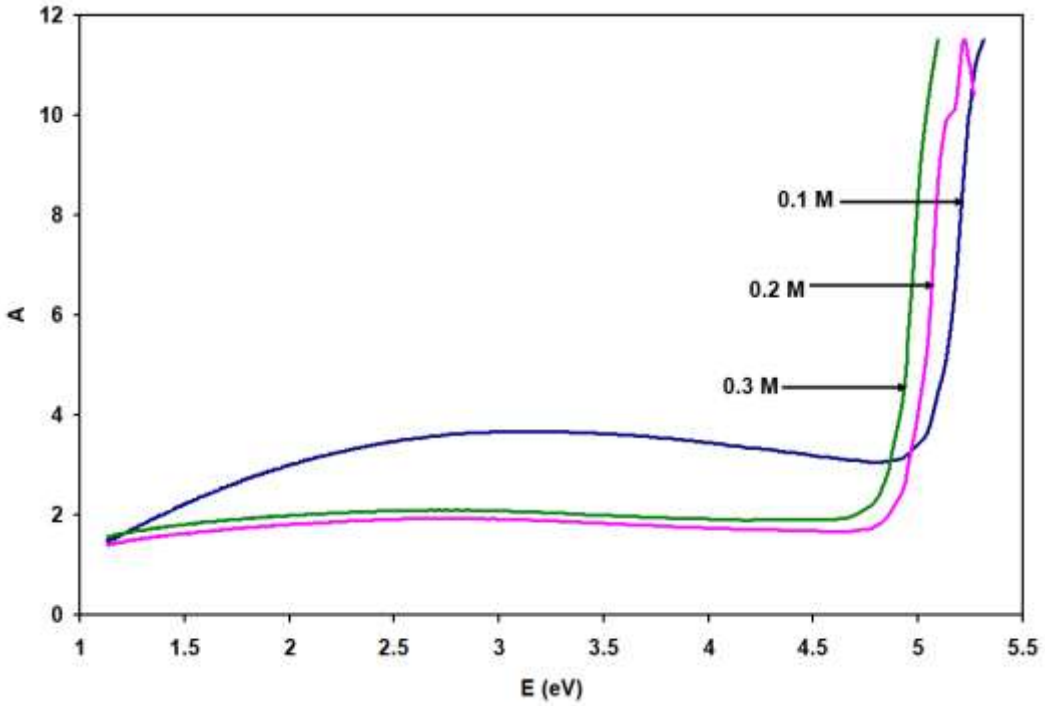

Figure 4.17: The absorption coefficient spectra for the $CdBr_2$ annealed at 400 °C powders at different concentration 0.1 M, 0.2 M, 0.3 M.

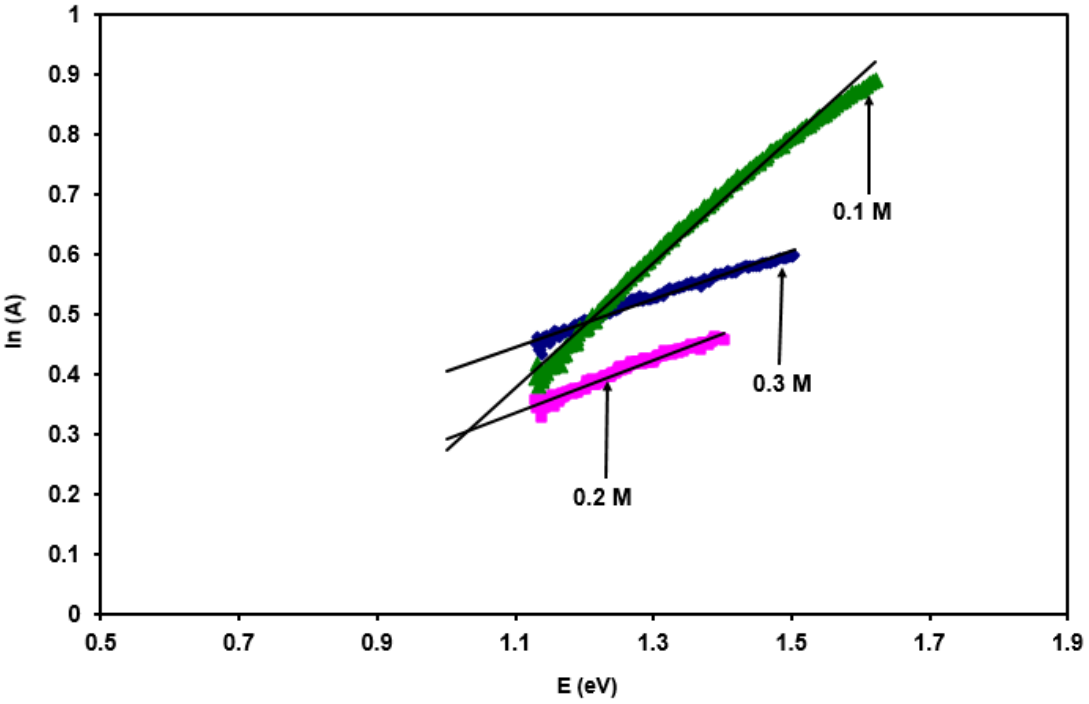

Figure 4.18: The $ln(A)-E$ variations $CdBr_2$ powders annealed at 400 °C for different concentration.

The energy gaps and energy band tails for all samples are shown in table 4.12. As can be noticed the values of the energy gaps decreased with increasing the annealed temperatures and also decreased with increasing the concentration of the samples. On the other hand, there is a consistency between table 4.11 (structural parameters) and table 4.12 (optical). As the annealed temperature is increased from 25 ^{o}C to 300 ^{o}C, the disorder D, ε, δ and SF% increased due to the high band tails energy which are observed at 300 ^{o}C. But for 400 ^{o}C the disorder D, ε, δ and SF% decreased. Hence, energy band tail decrease for annealed samples at 400 ^{o}C.

Table 4.12: The energy gaps and energy band tails for the $CdBr_2$ powders and the annealing powders at different concentrations.

Concentration	E_g				E_e	
	Powder	200 °C	300 °C	400 °C	300 °C	400 °C
0.1 M	5.40	5.10	5.00	5.10	2.02	2.96
0.2 M	5.35	4.95	4.90	4.91	2.69	2.29
0.3 M	5.09	4.87	4.81	4.85	4.74	2.50

4.3: Electrical properties.

To explore the electrical properties of the studied as prepared and annealed powder samples, Ag electrical contacts were located onto top and bottom of the samples. The ohmocity of the contacts was tested by verifying the linearity of the current-voltage characteristic curves. Fig. 4.19 shows the plots for all annealed powders. As can be seen from the figures, all curves are linear and follow Omh's law. Particularly, the electrical resistance can be measured from the reciprocal of the slope of linear parts of I-V characteristic.

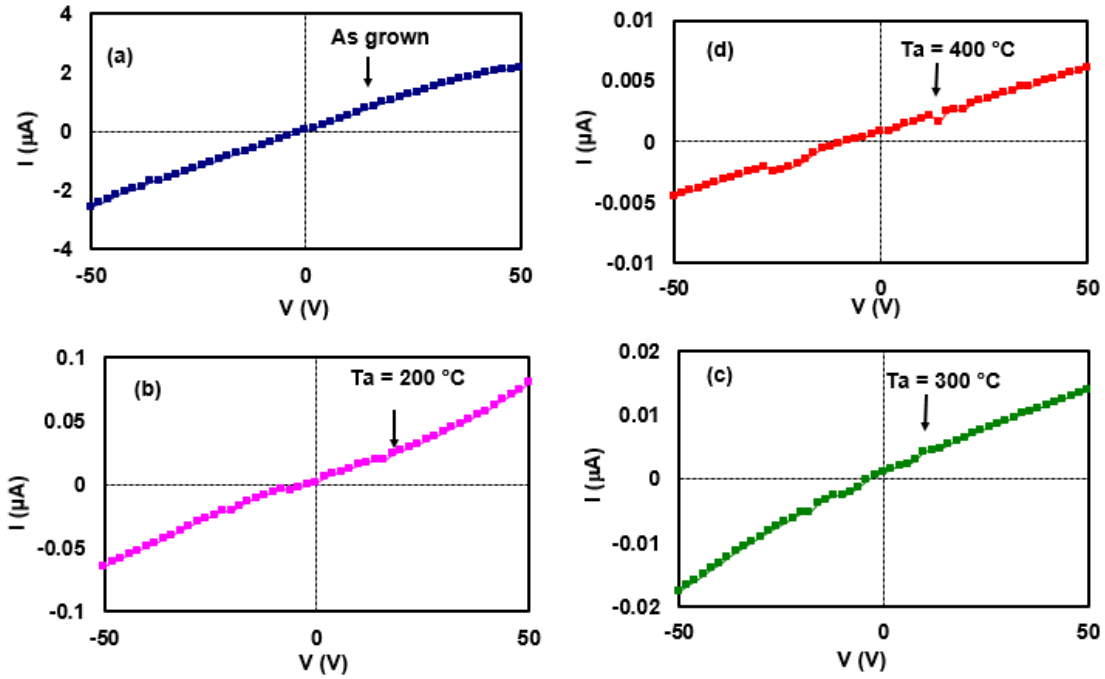

Figure 4.19: The I-V characteristic for the (a) as grown, (b) annealed at 200 °C, (c) 300 °C and (d) 400 °C of $CdBr_2$ powders.

The measured resistance for the unannealed and samples annealed at 200 °C, 300 °C and 400 °C are $2.7 \times 10^6\ \Omega$, $5.5 \times 10^8 \Omega$, $3.3 \times 10^9 \Omega$and $10 \times 10^9 \Omega$, respectively. As can be noticed, that the resistance is increased as the annealed temperatures increased. In addition, it is noticeable that the values of the current for the pure $CdBr_2$ powders are high when compared to the other current values of annealed powders (200 ^{o}C, 300 ^{o}C and 400 ^{o}C). The increase in the resistance value upon annealing the powders could be assigned to the phase transitions as we mentioned in the X-ray analysis.

The room temperature resistivity ($\rho = \frac{RA}{L}$) are also determined for all samples. Where R is the resistance, A the area and L is the thickness of the pressed samples. The calculated resistivity are $3.68 \times 10^6\ \Omega.cm$, $4.71 \times 10^8\ \Omega \cdot cm$, $2 \cdot 61 \times 10^{\ 9} \Omega \cdot cm$ and $8 \cdot 17 \times 10^9\ \Omega \cdot cm$ for the as grown, 200 ^{o}C, 300 ^{o}C and 400 ^{o}C powders, respectively. The increase in the electrical resistivity with increasing annealing temperature is assigned to the structural modifications.

4.4: Impedance Spectroscopy analyses.

To reveal the AC electrical properties of the as grown $CdBr_2$ powders and annealed powders, the top and bottom layer of pressed powders are imposed between terminals of impedance analyzer. The series capacitance (C_s) measurements are carried out in the frequency range of 10 to 1800 MHz. The series capacitance spectra are shown in Fig. 4.20. As seen from figure 4.20 (a), the capacitance spectra of the as grown $CdBr_2$ powders display an antiresonance followed by resonance peak at 469 MHz and 478 MHz, respectively. And also, another resonance followed by antiresonance peak appears at 1521 MHz and 1532 MHz, respectively. While the capacitance exhibits positive values in the frequency range of 473 MHz to 1527 MHz, it displays negative capacitance effect in the range of frequency of 434 MHz to 473 MHz. And in the range of 1528 MHz to 1795 MHz. After annealing the powders at 200 °C, 300 °C and 400 °C in rough vacuum atmosphere, the capacitance is strongly affected by annealing. As can be noticed from Fig. 4.20 (b), (c) and (d), the first antiresonance resonance peak disappeared when samples were annealed at 200 °C, and reappeared at 300 °C with small amplitude. When annealing temperature is raised to 400 °C, the peak disappeared. On the other hand, annealing the powders at 200 °C, 300 °C and 400 °C shifted the second resonance peak to 1107 MHz and to 1476 MHz and to 1719 MHz, and the antiresonance peak to 1116 MHz and to 1485 Hz and to 1728 MHz, respectively. The negative capacitance is now in the low range of frequency for annealed samples at 200 °C and 300 °C. In contrast, the negative capacitance for annealed sample at 400 °C is in high range of frequency.

Negative capacitance NC is a consequence of depopulation of interface states with stored charge or time dependent trap carrier recombination with increased potential [25]. NC is used for fast low power tunneling transistors [26]. NC is a concept exploiting ferroelectric materials integrated in fields effect transistors gates stacks in order to decrease the threshold swing and improve the drain

current therefore reach more energy efficient devices, operated at lower voltage [27]. From practical point of view achieving NC effect in $CdBr_2$ powder samples is of interest owing to the wide range of application in semiconductor device technology. NC effect is used to reduce noise and amplify signals [28-32]. It is also used as parasitic capacitance cancellers.

Literature data reported information about the existence of NC effect in semiconductor devices. It is believed that the terminals of the sample exhibit their own capacitance effect and the total capacitance is composed of three parts. One is the geometrical part and is supposed to be frequency invariant, the other is arising from holes oscillatory motion and the third is due to electrons. While the electrons charging process shown a positive effect which add to the geometrical capacitance, the holes capacitance have negative effect and is subtracted from the geometrical capacitance. The capacitance spectra will always display positive values when charging process is dominated by electrons. Under condition where much traps are available and behave as hole centers, the hole charging process dominated leading to a total negative capacitance effect [33-36].

Thus, the resonance is expected when electrons have sufficient time to follow incident AC signal and antiresonance appear when holes are able to follow AC signal. It can be thought that the position where resonance antiresonance take place is a center of switching from n to p type motion.

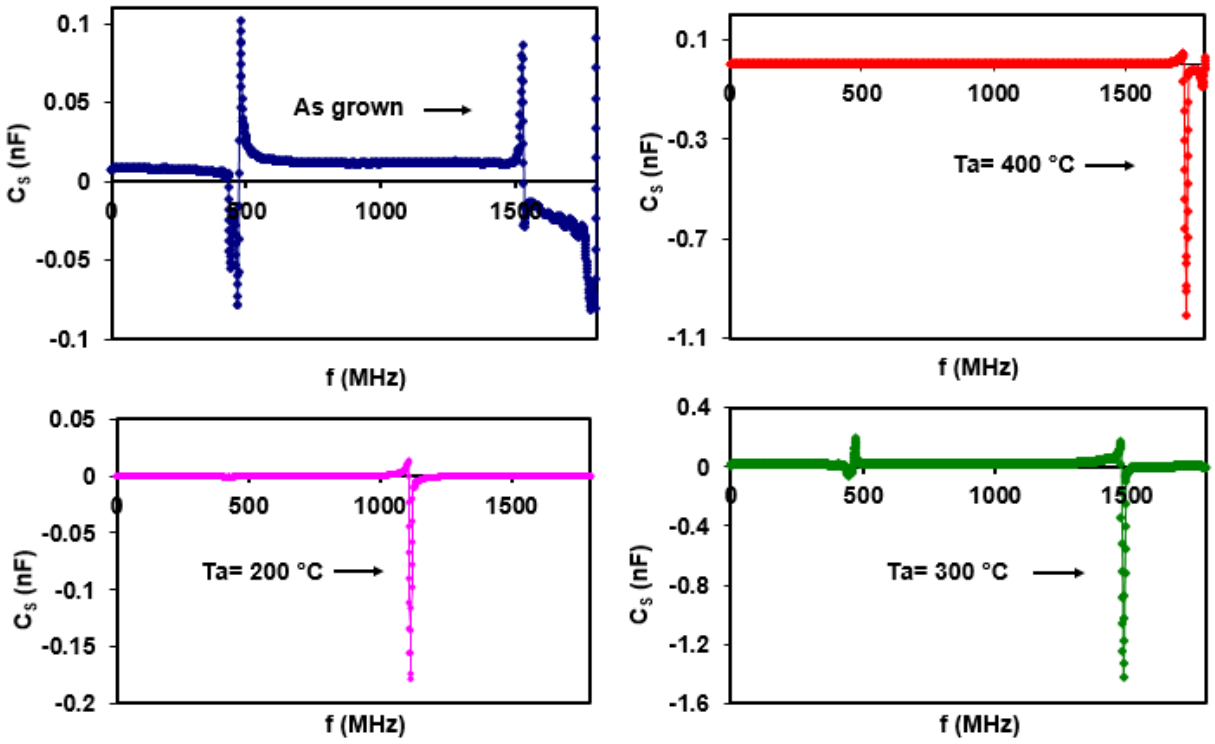

Figure 4.20: The series capacitance spectra for (a) as grown, (b) annealed at 200 °C, (c) 300 °C and (d) 400 °C of $CdBr_2$ powders.

Fig. 4.21 (a)- (d) shows the conductance spectra (G) for the as grown $CdBr_2$ and for annealed powders. It is clear that after annealing the behavior of the conductance spectra is varied with increasing the annealed temperature. Particularly, the conductance values decrease which reaches negative values with increasing the frequency at 470 MHz for all samples, G is more negative for as grown powders. G values for as prepared powders increase and become constant until frequency of 1340 MHz, then it is decreased to reach value of 0.08 Ω^{-1} at 1500 MHz. After that, it is increased to reach maxima of 0.092 Ω^{-1}. On the other hand, annealing the powders at 200 °C changes the behavior of the conductance and decreased its value. Clearly, (G) values above 1000 MHz reaches a maximum of 0.05 Ω^{-1} at 1150 MHz. For all frequencies above 1150 MHz, the conductance decreases with increasing the frequency signal. In addition, annealing the powders at 300 ^{o}C increases the values of the conductance. As can be seen from Fig. 4.20 (c), the conductance become

constant till 1300 MHz is reached. Then, increases to reach maxima of 2 Ω^{-1} at 1440 MHz. It is dramatically decreased from 2 Ω^{-1} to -1.1 Ω^{-1} when the frequency is 1450 MHz. Then G values increased gradually to reach value of 0.01 Ω^{-1}. Moreover, when annealed the powders at 400 ^{o}C are compared to that prepared powders it is clearly that they have the same behavior but different in G values. G values decreased slightly at frequency of 455 MHz, then it becomes a constant in the range of 500-1420 MHz. At 1500 MHz, G values decreased to reach value of -0.12 Ω^{-1}. After that it is increased to 0.05 Ω^{-1}. Negative conductance effect was previously observed in Se/Ag/Se stacked layers [22] and in operational transconductance amplifiers [37] such property is very important for producing integrated circuits beneficial for high speed data transmission [37]. Negative conductance is attributed to the trap effect which leads to coulomb repulsion and quantum interface [38].

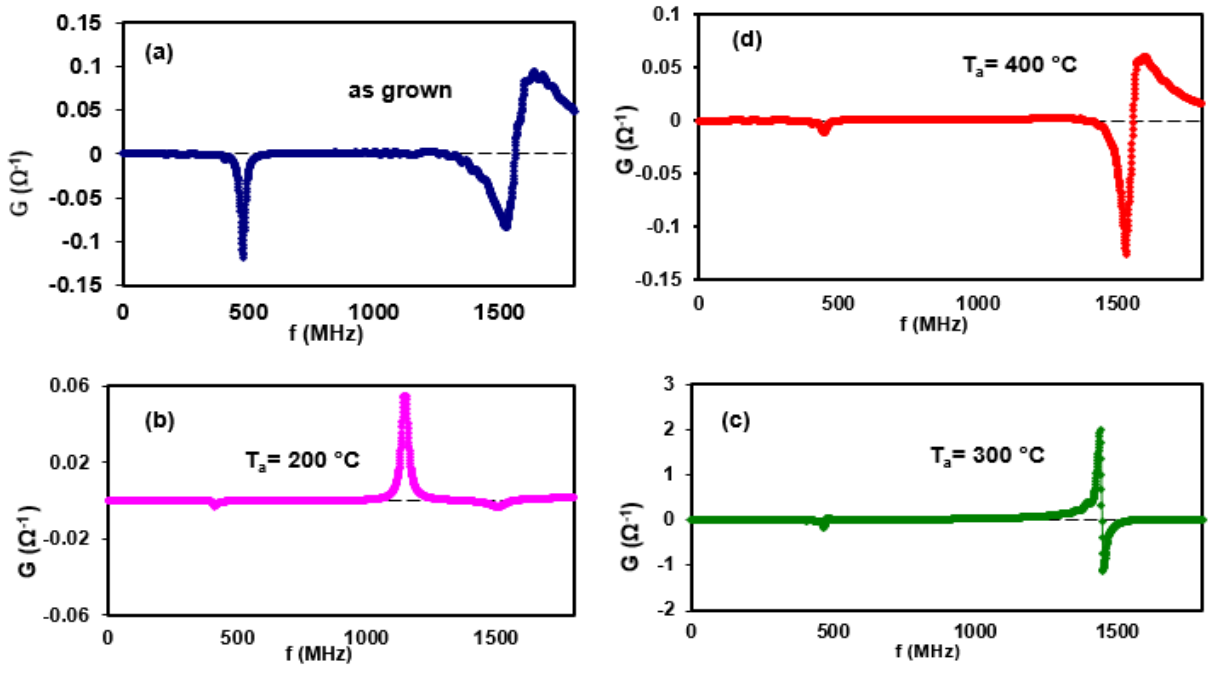

Figure 4.21: The conductance spectra for (a) as grown, (b) annealed at 200 °C, (c) 300 °C and (d) 400 °C of $CdBr_2$ powders.

Fig. 4.22 displays the impedance spectra for as grown and annealed $CdBr_2$ powders. As can be seen from the figure, the impedance for all samples decreases with increasing frequency. This behavior is expected because the capacitive reactance (X_C) decrease as the frequency (f) increase according to $\left(X_C = \frac{1}{2\pi f C}\right)$. The impedance values for the annealed powders are much higher than those of as grown ones and have the same behavior. It is due to the decreasing capacitance for annealed samples.

The impedance is strongly dependent on the resistance and capacitance values for this reason it shows minor and major peaks very similar to these of capacitance and conductance.

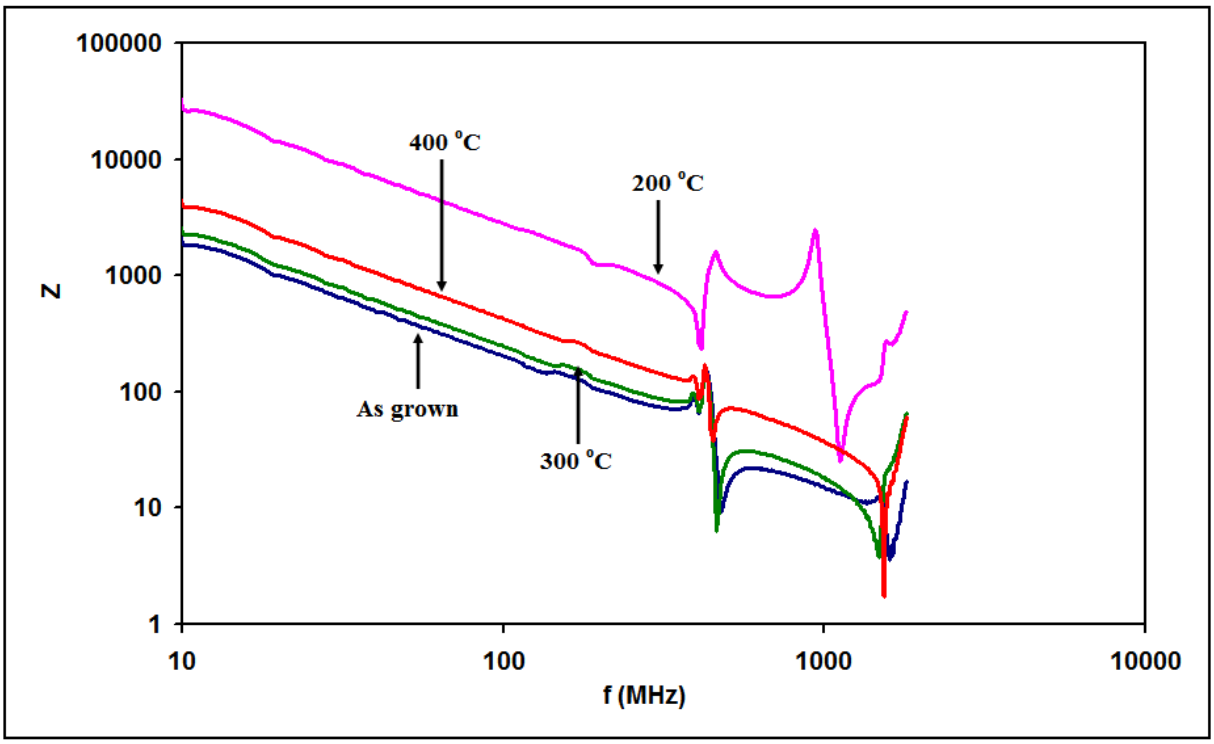

Figure 4.22: The impedance spectra for as grown, annealed at 200 °C, 300 °C, 400 °C of $CdBr_2$ powders.

The ability of the device to transmit and/or reject ac signals is determined from reflection coefficient (ρ). The Reflection coefficient $\left(\rho = \frac{Z_{device} - Z_{source}}{Z_{device} + Z_{source}}\right)$, which are calculated for the $CdBr_2$ as grown and annealed powders from the impedance values are displayed in Fig. 4.23. Generally, the Reflection coefficient takes values of -1 for shorts, stays negative for loads, zero for perfect matches and reaches +1 for open loads [39]. As can be noticed from figure, ρ values reaches value of +1 for all samples, and then ρ values slightly increased at frequency domain of 0-400 MHz. In the range of 520-1400 MHz, the reflection coefficient becomes constant for as grown and annealed samples at 300 °C and 400 °C. But for annealed at 200 °C the reflection coefficient remarkably decreased with increasing the frequency to reach value of 0.5 at 1143 MHz and then increased to 0.97 at 1247 MHz. In the remaining range of frequency, the reflection coefficient decreased for all samples. This results indicates that the samples behave as low-pass filter above 1.6 GHz.

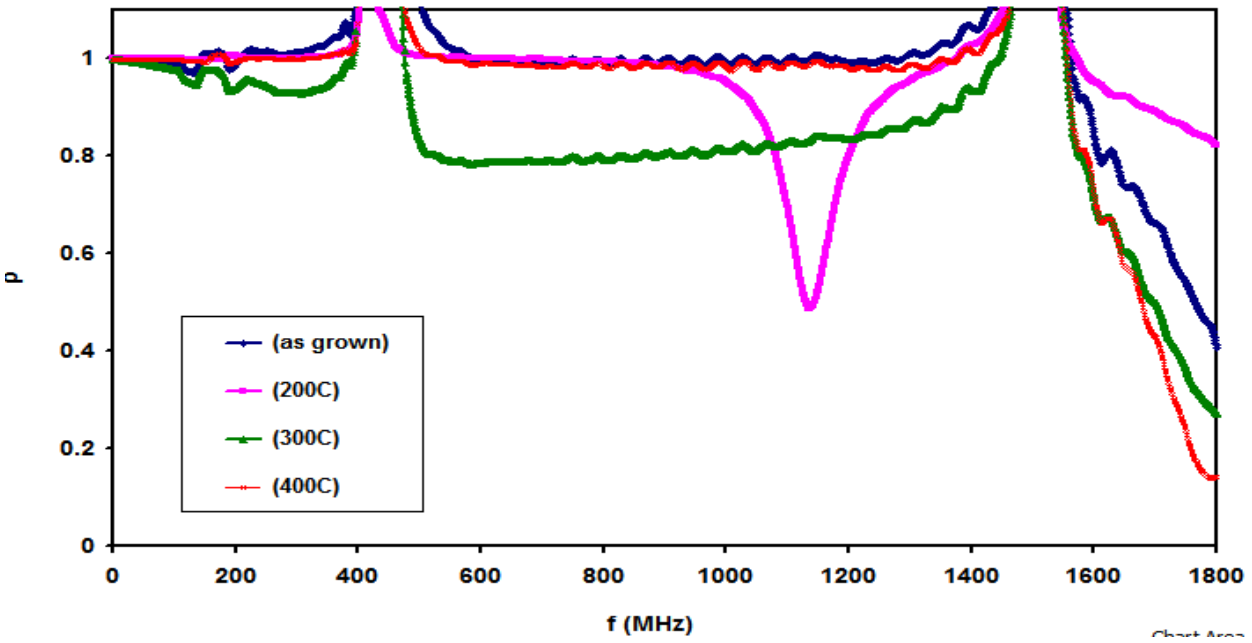

Figure 4.23: The reflection coefficient spectra for (a) as grown, (b) annealed at 200 °C, (c) 300 °C and (d) 400 °C of $CdBr_2$ powders.

Chapter 5

Conclusions

In this thesis we have studied the heating cycle, and heat treatment effects on the structural, optical and electrical properties of $CdBr_2$ powders. The powders were heated and in situ monitored by X-ray diffractometer. They were also annealed at temperatures of 200 °C, 300 °C and 400 °C. The structural investigations were carried out with the help of "TReor 92" and "Crystdiff " software packages. It was concluded that the heating of the powders and leaving it cool resulting enhancement of the hexagonal structure against triclinic. The structural parameters presented by microstrain, crystallite size, defect density and stacking faults percentage are all influenced by the heating processors. The other hand, when the $CdBr_2$ powders were heat treated, the weight of the phase triclinic phase slightly decreased exhibiting a structural phase transfer from triclinic to monoclinic at 400 °C. Except for the defects density. No remarkable effect was recorded on the structural parameters. But there is an increase in deformation disorder at 200 ^oC and 300 ^oC, and decreased for 400 ^oC.

From optical point of view, the $CdBr_2$ molar solutions display enhanced transparency upon increased solubility. The aqueous solution of the $CdBr_2$ display maximum transparency in the ultraviolet range and narrowed upon annealing reaching a value of 5.10 eV at 400 °C.

Electrically, the annealing increases the resistance of the samples due to the enhanced phase disorder. The capacitance, conductance and impedance spectra which was studied in the range of 0.01-1.8 GHz, displayed promising characteristic. Particularly, negative capacitance NC and negative conductance effect are observed in the radio wave and microwave ranges of frequency nominating the samples for use as band filters.

Even though the annealing enhances the physical properties of $CdBr_2$ leading to promising applications of the powders still further works are needed. More effective solutions must be brought into stage to overcome the problem of the existence of multiphase in the samples. For this reason, one of our future works is to try longer annealing time or larger annealing temperature.

References:

[1] Grzesiak-Nowak, M., Appleby, G., & Łasocha, W. (2015). Powder diffraction and synchrotron radiation, a powerful tool in the investigation of new compounds: CdBr2 (3-fluoroaniline) 2 and CdBr2 (4-fluoroaniline) 2. X-Ray Spectrometry, 44(5), 398-403.

[2] Zou, S., Yang, G., Pang, T., Zou, M., Liu, R., Chen, B., … & Zou, B. (2018). One-step synthesis of nail-like Mn-doped CdS/CdBr2 hetero-nanostructures for potential lasing application. Nanotechnology, 30(7), 075605.

[3] Boopathi, K., Babu, S. M., Jagan, R., Athimoolam, S., & Ramasamy, P. (2018). Synthesis, crystal growth, physio-chemical characterization and quantum chemical calculations of NLO active metal–organic crystal: dibromo (4-hydroxy-l-proline) cadmium (ii) for non-linear optical applications. New Journal of Chemistry, 42(21), 17464-17477.

[4] Prakash, J. T. J., & Gnanaraj, J. M. S. (2015). Growth and characterization of Cadmium Thiosemicarbazide Bromide crystals for antibacterial and nonlinear optical applications. Spectrochimica Acta Part A: Molecular and Biomolecular Spectroscopy, 135, 25-30.

[5] Liang, F., Kang, L., Lin, Z., & Wu, Y. (2017). Mid-infrared nonlinear optical materials based on metal chalcogenides: structure–property relationship. *Crystal Growth & Design*, *17*(4), 2254-2289.

[6] Deswal, S., Singh, S. K., Rambabu, P., Kulkarni, P., Vaitheeswaran, G., Praveenkumar, B., ... & Boomishankar, R. (2019). Flexible Composite Energy Harvesters from Ferroelectric A2MX4 type Hybrid Halogenometallates. Chemistry of Materials.

[7] Greenhalgh, R. C., Tsai, V., Abbas, A., Kornienko, V., Fiducia, T. A. M., Togay, M., ... & Barth, K. L. (2019, June). Analysis of MZO/CdTe photovoltaic device treated with cadmium bromide. In 2019 IEEE 46th Photovoltaic Specialists Conference (PVSC) (pp. 2489-2493). IEEE.

[8] Lide, D.R. CRC Handbook of Chemistry and Physics 88TH Edition 2007-2008. CRC press, Tayler & Francis, Boca Raton, FL 2007, p. 4-53.

[9] Williams, R. T., & Yen, W. M. Excitonic Processes in Condensed Matter, EXCON'98, Boston 1998. *Electrochem. Soc. Proc. Ser., PV*, *98*(25), p.450.

[10] Kittel, C., McEuen, P., & McEuen, P. (1996). *Introduction to solid state physics* (Vol. 8, p. 105-130). New York: Wiley. P. 4-9.

[11] Al Garni, S. E., & Qasrawi, A. F. (2017). Effect of Indium nano-sandwiching on the structural and optical performance of ZnSe films. *Results in physics*, *7*, 4168-4173.

[12] F. Humphreys and M. Hatherly, Recrystallization and Related Annealing Phenomena, second edition. Kidlington, Oxford: Elsevier Ldt.

[13] Springer handbook of Electric and Photonic Materials, Safa Kasap, Peter Capper Editors. 2nd edition. Page 56-58.

[14] Jim clark, Physical and Theoretical Chemistry Textbook (2004). The Beer-Lambert Law. Libretexts.

[15] Hassanien, A. S., & Akl, A. A. (2016). Effect of Se addition on optical and electrical properties of chalcogenide CdSSe thin films. *Superlattices and Microstructures*, *89*, 153-169.

[16] Atrens, A., Song, G. L., Shi, Z. M., Soltan, A., Johnston, S., & Dargusch, M. S. (2018). Understanding the corrosion of Mg and Mg Alloys Encyclopedia of Interfacial Chemistry: Surface Science and Electrochemistry. vol 6. ed K Wandel.

[17] Sergey N. Makarov, Reinhold Ludwig, Stephen J. (2019) Bitar. Practical Electrical Engineering.

[18] Arendse, C. J., D. Knoesen, and D. T. Britton. "Thermal stability of hot-wire deposited amorphous silicon." *Thin Solid Films* 501, no. 1-2 (2006): 92-94.

[19] Park, Jong-Tae, and Jerzy A. Szpunar. "Effect of initial grain size on texture evolution and magnetic properties in nonoriented electrical steels." *Journal of Magnetism and Magnetic Materials* 321, no. 13 (2009): 1928-1932.

[20] Fellah, Mamoun, Naouel Hezil, Mohamed Zine Touhami, Aleksei Obrosov, Sabine Weiß, Egor B. Kashkarov, Andrey M. Lider, Alex Montagne, and Alain Iost. "Enhanced structural and tribological performance of nanostructured Ti–15Nb alloy for biomedical applications." *Results in Physics* 15 (2019): 102767.

[21] Servidori, M., Z. Šourek, and S. Solmi. "Some aspects of damage annealing in ion-implanted silicon: Discussion in terms of dopant anomalous diffusion." *Journal of applied physics* 62, no. 5 (1987): 1723-1728.

[22] Qasrawi, A. F., and Hadil D. Aloushi. "Formation, negative capacitance and negative conductance effects in Selenium stacked layers sandwiched with Ag nanosheets." *Materials Research Express* 6, no. 8 (2019): 086435.

[23] Singh, P. K., Shukla, N., Rao, V., & Dwivedi, D. K. (2020). Effect of Annealing on the Structural and Optical Properties of Amorphous Ge8Se60Te30Sb2 Thin Films. *Advanced Science, Engineering and Medicine*, *12*(1), 31-35.

[24] A. F. Qasrawi, M. F. Taleb, (2019). Effect of Y, Au and YAu Nano sandwiching on the structural, optical and dielectricproperties of ZnSe thin films. Vol. 16, No. 3, March 2019, p. 95 – 105.

[25] Bhattacharjee, S., Banerjee, A., Mazumder, N., Chanda, K., Sarkar, S., & Chattopadhyay, K. K. (2020). Negative capacitance switching in size-modulated Fe 3 O 4 nanoparticles with

spontaneous non-stoichiometry: confronting its generalized origin in non-ferroelectric materials. *Nanoscale*, *12*(3), 1528-1540.

[26] Li, H., Liang, J., Xu, P., Luo, J., & Liu, F. (2020). Vertically stacked SnSe homojunctions and negative capacitance for fast low-power tunneling transistors. *RSC Advances*, *10*(35), 20801-20808.

[27] Bellando, F., Dabhi, C. K., Saeidi, A., Gastaldi, C., Chauhan, Y. S., & Ionescu, A. M. (2020). Subthermionic negative capacitance ion sensitive field-effect transistor. *Applied Physics Letters*, *116*(17), 173503.

[28] Kwon, Daewoong, Korok Chatterjee, Ava J. Tan, Ajay K. Yadav, Hong Zhou, Angada B. Sachid, Roberto Dos Reis, Chenming Hu, and Sayeef Salahuddin. "Improved subthreshold swing and short channel effect in FDSOI n-channel negative capacitance field effect transistors." *IEEE Electron Device Letters* 39, no. 2 (2017): 300-303.

[29] Qasrawi, Atef Fayez. "Characterization of Au/As2Se3 Multifunctional Tunneling Devices." *physica status solidi (a)* 217, no. 5 (2020): 1900899.

[30] Mehta, Hema, and Harsupreet Kaur. "Study on impact of parasitic capacitance on performance of graded channel negative capacitance SOI FET at high temperature." *IEEE Transactions on Electron Devices* 66, no. 7 (2019): 2904-2909.

[31] Ku, Hansol, and Changhwan Shin. "Transient response of negative capacitance in P (VDF 0.75-TrFE 0.25) organic ferroelectric capacitor." *IEEE Journal of the Electron Devices Society* 5, no. 3 (2017): 232-236.

[32] Park, Hyeon Woo, Jangho Roh, Yong Bin Lee, and Cheol Seong Hwang. "Modeling of negative capacitance in ferroelectric thin films." *Advanced Materials* 31, no. 32 (2019): 1805266.

[33] Niu, Quan, N. Irina Crăciun, Gert-Jan AH Wetzelaer, and Paul WM Blom. "Origin of negative capacitance in bipolar organic diodes." *Physical Review Letters* 120, no. 11 (2018): 116602.

[34] Khanfar, Hazem K., A. F. Qasrawi, and Sufyan R. Shehada. "Negative Capacitance Effect in Ag/α-In 2 Se 3/CdS/CdSe/C Dual Band Stop Filters." *Journal of Electronic Materials* 48, no. 1 (2019): 244-251.

[35] Khanfar, Hazem K., A. F. Qasrawi, and Sufyan R. Shehada. "Negative Capacitance Effect in Ag/α-In 2 Se 3/CdS/CdSe/C Dual Band Stop Filters." *Journal of Electronic Materials* 48, no. 1 (2019): 244-251.

[36] Yalcin, Mesut, and Fahrettin Yakuphanoglu. "Voltage and frequency dependence of negative capacitance behavior in a Graphene-TiO2 nanocomposite photoanode based on quantum dot sensitized solar cells." *Optik* 183 (2019): 1099-1105.

[37] Rambabu, Sirikonda, Alak Majumder, and Abir J. Mondai. "A 90nm gain enhanced modified cascode ota structure with positive feedback." In *2017 2nd International Conference on Communication and Electronics Systems (ICCES)*, pp. 203-207. IEEE, 2017.

[38] Dorn, Gerhard. "A Born-Markov master equation approach to correlated quantum systems in non-equilibrium." (2015).

[39] A. F. Qasrawi, (2018). Formation and negative capacitance effect in Au/Bi2O3/ZnS/Ag heterojunctions designed as microwave resonators.

ملخص الرسالة

اثار المعالجة الحرارية والتشخيص الحيوي لتحولات الطور في بودرة الكاديوم بروماید

الطالبة امال مصطفى نجاح وشاحي

المشرف البروفيسور الدكتور عاطف قصراوي

في هذه الرسالة ، ركزنا على دراسة تأثيرات التسخين و التلدين في الطور، على الخصائص التركيبية والبصرية والكهربائية لبودرة الكاديوم بروماید ($CdBr_2$). تم تعريض الكاديوم بروماید لعمليات تسخين في نطاق درجة حرارة 20-200 درجة مئوية. بالنسبة لهذه العينات ، قبل التسخين ، كانت هناك تراكيب بلورية متعددة. التركيب البلوري الأكثر شيوعًا هو التركيب الثلاثي الميول. أدت دورة التسخين إلى استرخاء المعاملات الهيكلية البلورية وتغيير التركيب السائد من ثلاثي الميل إلى سداسي.

يترافق مع تغيير الهيكل تغيرات في حجم البلورة ، والانفعال ، وكثافة الخلل وزيادة نسبة أخطاء التراص . من ناحية أخرى ، عندما تمت معالجة بودرة $CdBr_2$ بالحرارة عند درجات حرارة مرتفعة تبلغ 200 درجة مئوية و 300 درجة مئوية و 400 درجة مئوية لمدة ساعة واحدة في وسط مفرغ الهواء. كانت الخصائص الهيكلية مختلفة. وبالتحديد ، انخفض وزن طور الهيكل ثلاثي الميل من 68.3٪ إلى 53.9٪ و 46.0٪ ووصل إلى 13.7٪ حيث زادت درجة حرارة التلدين من 25 درجة مئوية إلى 200 درجة مئوية و 300 درجة مئوية ووصلت إلى 400 درجة مئوية على التوالي. كان التركيب الهيكلي الأكثر شيوعًا للعينات الملدنة عند 400 درجة مئوية أحادية الميل .غيّرت دورة التلدين المعاملات البلورية ، وعززت بشكل طفيف حجم البلورة والإنفعال المجهري. كما تم تقليل كثافة الخلل دون تغيير نسب خطأ التكديس .أظهرت الفحوصات الضوئية على العينات قبل و بعد المعالجة بالحرارة أن شفافية المساحيق في نطاق الأشعة فوق البنفسجية تزداد بزيادة التركيز المولي وزيادة درجة حرارة التلدين. انخفضت فجوة نطاق الطاقة من 5.11 فولت إلى 5.10 فولت حيث زادت درجة حرارة التلدين من 25 درجة مئوية إلى 400 درجة مئوية .أظهرت القياسات الكهربائية أن عملية التلدين تزيد من المقاومة الكهربائية للعينات المتطابقة.

بينما أظهرت العينات قبل المعالجة بالحرارة ذروتين للرنين المضاد في نطاقات الطيف الراديوي والميكروويف ، أظهرت العينات الملدنة عند 200 درجة مئوية و 400 درجة مئوية ذروة واحدة في نطاق الميكروويف. كلما ارتفعت درجة حرارة التلدين ، زاد تردد الرنين. يعرض أطياف السعة القيم السالبة بالقرب من قمم الرنين. على الدوام ، تُظهر أطياف التوصيل تأثيرًا سلبيًا للتوصيل يشير إلى سيطرة عملية االعبور النفقي في العينات الملدنة. أظهرت قياسات حجم معامل الانعكاس للبودرة و العينات الملدنة في نطاق الميكروويف إمكانية تطبيق العينات كمرشحات تمرير النطاق تعمل فوق 1.5 جيجا هرتز.